

Review

# Review on Sensing Applications of Perovskite Nanomaterials

Muthaiah Shellaiah  and Kien Wen Sun \*

Department of Applied Chemistry, National Chiao Tung University, Hsinchu 30010, Taiwan;  
muthaiah1981@nctu.edu.tw

\* Correspondence: kwsun@mail.nctu.edu.tw

Received: 26 June 2020; Accepted: 11 July 2020; Published: 14 July 2020



**Abstract:** Recently, perovskite-based nanomaterials are utilized in diverse sustainable applications. Their unique structural characteristics allow researchers to explore functionalities towards diverse directions, such as solar cells, light emitting devices, transistors, sensors, etc. Many perovskite nanomaterial-based devices have been demonstrated with extraordinary sensing performance to various chemical and biological species in both solid and solution states. In particular, perovskite nanomaterials are capable of detecting small molecules such as O<sub>2</sub>, NO<sub>2</sub>, CO<sub>2</sub>, etc. This review elaborates the sensing applications of those perovskite materials with diverse cations, dopants and composites. Moreover, the underlying mechanisms and electron transport properties, which are important for understanding those sensor performances, will be discussed. Their synthetic tactics, structural information, modifications and real time sensing applications are provided to promote such perovskite nanomaterials-based molecular designs. Lastly, we summarize the perspectives and provide feasible guidelines for future developing of novel perovskite nanostructure-based chemo- and biosensors with real time demonstration.

**Keywords:** perovskite; nanomaterials; hybrid materials; chemosensory; bioanalyte detection; transistors; electron transport; nanocomposites; real time application

## 1. Introduction

Development of nanomaterials for diverse analyte detection with respect to environmental and biosafety measures are becoming essential [1–3]. Wherein, the species recognition can be identified by miscellaneous responses like colorimetric, spectrometry, voltammetry and morphological changes [4–8]. Among the reported nanomaterials, perovskites are exceptional hybrid materials with variety of applications, such as solar cells, light emitting devices, transistors, sensors, etc. [9–14]. The compounds that have the ABX<sub>3</sub> formula type with differently sized ‘A’ and ‘B’ cations bind to anion X are known as perovskite [15]. These perovskites are classified in three categories: inorganic oxide perovskites, alkaline metal halide perovskites and organic metal halide perovskites with oxide or halide anions [16,17]. Moreover, they can be synthesized from zero to three dimensional nanostructures and consumed in many sustainable applications [18–20]. Among these applications, sensory utilities using perovskite nanomaterials to attain the signals to specific analyte in solid or solution states have attracted most attention [21,22].

Perovskites with general formula ABO<sub>3</sub> display good thermal stability with a 3–4 eV band gap, hence were consumed in many gas sensing studies [23]. Semiconducting properties of these nanocrystalline perovskites allow the detection of gaseous species by means of current–voltage (I–V) responses [24]. For instance, Wang et al. established the LaFeO<sub>3</sub> nanocrystalline perovskite towards the discovery of carbon dioxide (CO<sub>2</sub>) gas [25]. Metal halide/hybrid perovskites were also applied in many analytes sensing by detecting changes in phosphorescence, fluorescence, I–V fluctuations,

morphological, etc. [26]. Metal halide/hybrid perovskite nanomaterials also have the advantage of providing the sensory responses to analyte in solution and solid states [26,27]. However, stability of metal halide perovskite-based sensors can be affected by various factors, such as solvents, moisture, time and temperature [28]. Similarly, the diverse crystalline structures of metal halide perovskites like cubic, tetragonal and orthorhombic may play a vital role in sensory studies [29]. Therefore, an in-depth discussion is required for the upcoming research designs on metal halide perovskite-based sensors.

Doping or mixing of other nanostructures/ions over perovskites tends to form a nanocomposite like structure, which can be further utilized as sensors [30]. For example, Cho and coworkers recently demonstrated the humidity sensing capability of the  $\text{CsPb}_2\text{Br}_5/\text{BaTiO}_3$  composite [31]. Other than its potential sensory application, a one-step aerosol deposition (AD) process was explored to develop such a nanocomposite powder. In a similar fashion, manganese (Mn)-doped halide perovskite nanomaterials showed an exceptional semiconducting property and sensing ability [32]. Lin et al. demonstrated the Mn-doped  $\text{CsPbCl}_3$  nanocrystals towards the sensing of oxygen ( $\text{O}_2$ ) by means of host-dopant energy transfer [33]. This kind of photoluminescence (PL)-based sensory design has extensively been researched. Many procedures have been explored to develop perovskite nanomaterials, including chemical synthesis, ball-milling, combustion synthesis, sputtering, sol-gel, solid-state reaction, etc. [34–40]. Moreover, it now becomes essential for finding applications of perovskite nanomaterials in sustainable research, such as solar cells, light emitting devices, transistors and sensors.

In this review, valuable information on sensory applications of perovskite nanomaterials (Figure 1) is provided. The mechanisms and electron transport properties of these sensor matrixes are described. In the end, the material synthesis, structural modifications, and real time applications are defined along with their developing scopes in the near future.

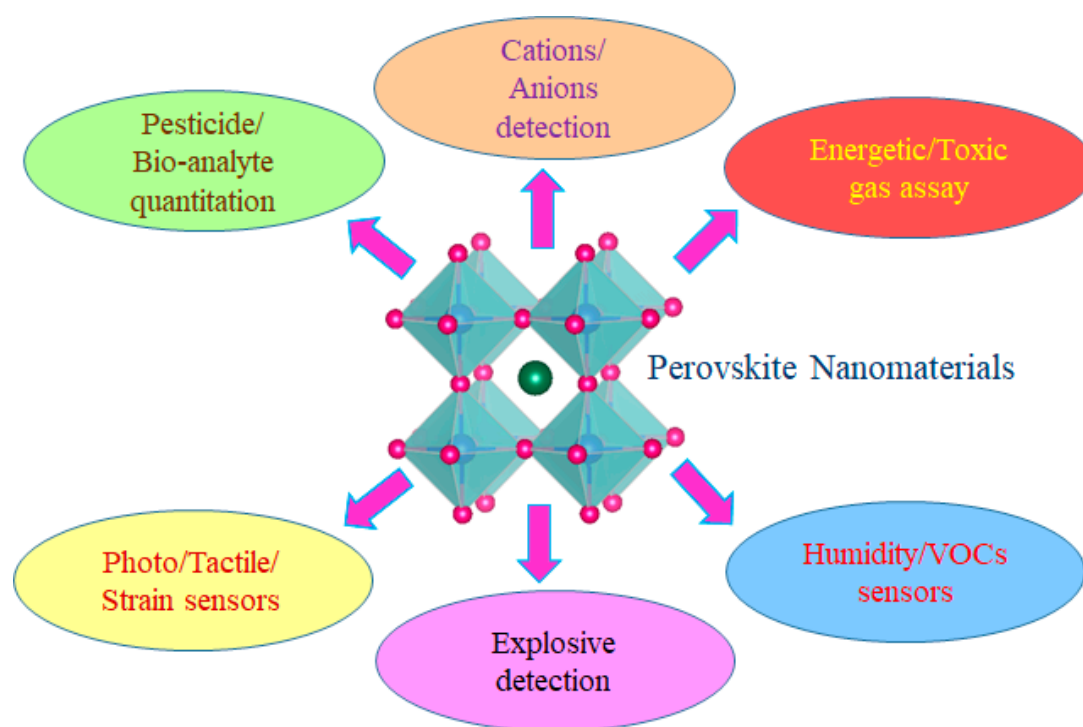


**Figure 1.** Schematic illustration of the sensory applications of perovskite nanomaterials.

## 2. Structure, Stability and Properties of Perovskites

Perovskites with  $\text{ABX}_3$  formula exist in a undistorted cubic structure with 6-fold coordinated smaller B cation enclosed by an octahedron of anions, which are further 12-fold cuboctahedral coordinated with a larger A cation as shown in Figure 2. Metal oxide perovskites exist in three-dimensional frameworks with corner-sharing  $\text{BO}_6$  octahedra, whereas halide ions are considered

instead of oxygen atoms in metal halide perovskites. Above the cubic structure can be distorted by tilting and altering the octahedra by cation displacements, which leads to reduced symmetries like orthorhombic, tetragonal and trigonal. In fact, the metal oxide perovskites seem to be stable with the cubic structure, but they also require a Goldschmidt's tolerance factor with values between 0.9 and 1. The tolerance factor has been derived from  $t = (R_A + R_X)/\sqrt{2} (R_B + R_X)$ , here  $R_A$ ,  $R_B$ , and  $R_X$  are the ionic radii of ions presented in respective A, B and X sites [41]. If the tolerance factors of the perovskite materials have a value between 0.7 and 0.9, they could have a distorted cubic structure, which result in reduced symmetries. Apart from the above factors, the stability of many metal halide perovskites is also affected by other factors, such as temperature, water and the environment as described subsequently.

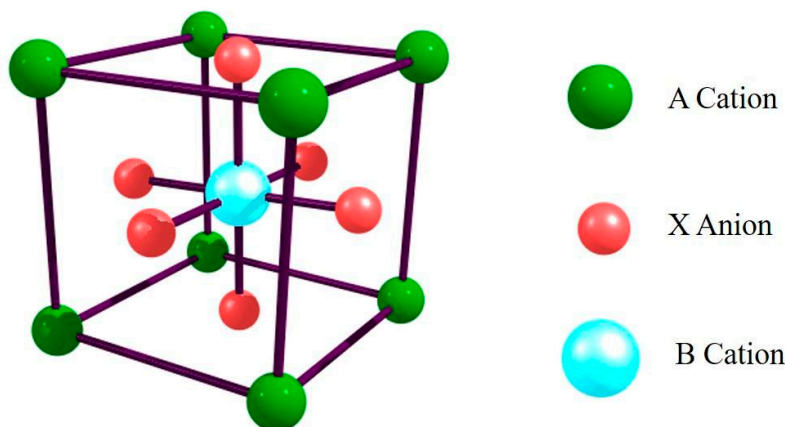


**Figure 2.** Undistorted cubic structure of perovskites with general formula  $ABX_3$ .

Since annealing is an important step in the fabrication processes of metal halide perovskites for sustainable applications, it is necessary to identify the effective operation temperatures. During this annealing process, the majority of metal halide perovskites might experience phase transitions. For example, with a temperature range of 300–600 K, the symmetries of  $CsPbX_3$  ( $X = Cl, Br$  and  $I$ ) are altered to monoclinic, orthorhombic, tetragonal or cubic via phase transitions [42–44]. In contrast, temperature stability of organic–inorganic hybrid perovskites is rather poor and the perovskites could decompose at higher temperatures. For instance,  $CH_3NH_3PbX_3$  ( $X = Cl, Br$  and  $I$ ) displayed several phase transitions (cubic, tetragonal and orthorhombic) while operating the temperature from 140 to 400 K [45–49]. However, the thermally induced phase transitions of metal/hybrid halide perovskites can also increase their practical use as temperature sensors.

The stability of perovskites is mostly affected by water, which cause the dissolution/degradation of materials during the fabrication process. In the case of metal oxide perovskites, they tend to form hydroxyl ions ( $OH^*$ ) over their surface with water, which is currently applied in the water splitting application [50]. On the other hand, in the presence of water, the metal halide perovskites may degrade due to the distortion of their lattice sites. Likewise, organic–inorganic hybrid metal halide perovskites were also affected by the existence of water molecules. For example, the  $CH_3NH_3PbI_3$  decomposed into  $CH_3NH_3 I$  and  $PbI_2$  when encountered with the water molecules [51]. However, such degradation was also extensive in supportive environment.

Moisture environment or organic solvents in their gaseous state also significantly affect the stability of perovskite materials [52,53]. The stability of perovskite materials was considerably disturbed when exposed in a gaseous environment, such as  $NO_2$ ,  $CH_4$ ,  $NH_3$ ,  $C_2H_5OH$ , acetone, etc. [26], as a result, they can be used as sensors for those gaseous species. The abrupt changes in these perovskite materials can be recorded through chemiresistive I–V, phosphorescence and fluorescence responses. Nevertheless, the opto-electronic properties of perovskites play a vital role in these sensing studies.

Perovskite oxides are well known candidates with exceptional properties, such as electrical conductivity, ferroelectricity, superconductivity, catalytic activity, etc. For example, the studies

on the ferroelectricity of BaTiO<sub>3</sub> indicated that it was strongly related to the crystal structure [54]. With increasing temperature, the BaTiO<sub>3</sub> underwent three phase transitions from monoclinic to tetragonal and cubic structure. However, above 303 K, the ferroelectric property disappeared due to the crystallization in the cubic structure. These changes in ferroelectricity as a function of temperature can be utilized in temperature sensors. Similar to the ferroelectricity, these oxide perovskites were also demonstrated as superconductors at certain temperatures, hence provides possible applications in temperature detection. Due to excess oxygen content [55,56], perovskite oxides like LaCoO<sub>3</sub>, LaFeO<sub>3</sub> and LaMnO<sub>3</sub> displayed exceptional hole conductivity (as high as  $\sigma = 100$  S/cm), hence were currently used as cathodes in solid oxide fuel cells (SOFCs). In a similar fashion, perovskites are the materials capable of producing piezoelectricity, which has been well recognized through many sensory applications, such as pressure sensor, force sensor, strain gauge, actuators, etc. [57]. Oxide perovskites also possess the multiferroicity characteristic, and thus become the excellent materials for memory devices and sensors [58]. The promising catalytic activity of metal oxide perovskites has been demonstrated in various reactions. Due to the presence of a large number of oxygen vacancies or deficiency sites on the surface, metal oxide perovskites are recognized as an oxygen active catalyst or activated model sites [59], which allows the researchers to utilize them in the reaction-based sensory readings.

Similar to the metal oxide perovskites, the metal/hybrid halide perovskites also possess the diverse opto-electronic properties that play a vital role in many sustainable applications. Specified reviews are available to understand their optical and electrical properties [60,61]. Tuning the stoichiometries of halides (Cl, Br and I) and metal ions can lead to different material properties and crystalline structures. Metal/hybrid halide perovskites displayed blue, green and red photoluminescence properties were achieved by varying the stoichiometries of either metal or halide ions [62]. The absorption and PL of halide perovskites are extremely sensitive to the temperature and pressure. In particular, temperature change may induce phase transitions and influence exciton–phonon interactions via thermal expansion. Similarly, ferroelectric properties of halide perovskites have been investigated in many reports [63]. Enhancement in photovoltaic properties by means of ferroelectric domain structures in MAPBI<sub>3</sub> was demonstrated by Yam and coworkers [64]. Good electron and hole transporting properties of organometallic halide perovskites [65] have directed researchers towards electrical sensory investigations. Moreover, better understanding the charge-carrier dynamics is important to improve their optical properties as well [66].

### 3. Factors Affecting Sensor Interrogations of Perovskite Nanomaterials

Sensory utilities of perovskite nanomaterials can be affected by the following factors, hence the design of suitable nanostructures towards a specific direction must be done with the consideration of these elements.

- A. Suitable nanostructure: Design and development of suitable nanostructure for a specified analyte/sensor utility is still a question to researchers. Since perovskites may form diverse nanostructures such as quantum dots, nanocrystals, nanowires/rods, nanoparticles, etc. It is still the most difficult challenge for scholars to identify the proper perovskite nanomaterials for their target sensor investigation. Another critical issue is that some synthetic path may lead to a mixture of nanostructures, hence an improved strategy or synthetic path is required to afford explicit nanostructured materials.
- B. Stability: perovskite nanomaterials has the major issue of stability, which might influence many sensor responses. For example, organometallic halide perovskites can be significantly affected by moisture and humid conditions. Likewise, both oxide and halide perovskites can become unstable by temperature, pressure and solvent environment [67]. However, this property may also direct the perovskite materials toward sensors for pressure, temperature, solvents, etc. [68–70]. These factors might disrupt their crystallinity, structure and morphology, hence

sensory designs for other analytes require precautions. Due to the stability concern, recycle of perovskite nanomaterials is still an open question in electronic device-based sensors.

- C. Toxicity/environmental affordability: to authenticate the sensor efficacies of perovskite nanomaterials, elucidation of their toxicity or environmental affordability is much anticipated. Toxicity measurements may tell us the biocompatibility of those materials to be consumed in healthcare products. However, majority of halide perovskites are likely to be toxic, hence their use in biosamples are rather restricted. For example,  $\text{CH}_3\text{NH}_3\text{PbX}_3$  ( $X = \text{Cl}, \text{Br}$  and  $\text{I}$ ) are well known candidates with good emissive nature but should be avoided to use in biosamples. Bio/environmental samples may be affected by the presence of toxic Pb ions, hence actions are needed to eliminate their harmfulness via suitable modifications with appropriate capping or cations [71].
- D. Quantum yield ( $\Phi$ ): consumption of luminescent perovskite nanomaterials-based analyte detection is becoming the modern research topic. However, developing such luminescent materials with analyte specificity is still a challenge. Since luminescent property may vary at diverse precursor dilution [72], it is very essential to develop materials with high quantum yield ( $\Phi$ ) values. For example, Zhu et al. publicized the  $\text{CsPbBr}_3$  perovskite nanocrystals with 87% quantum yield towards colorimetric sensing of peroxide number in edible oils [73]. Therefore, the development of luminescent perovskite nanomaterials with high quantum yield is expected for sensor studies.

#### 4. Sensing Utilities of Metal Oxide Perovskite Nanomaterials

Until now, many semiconducting perovskites have been reported in a variety of gas sensing studies, which can be applied in environmental, fire and vehicle monitoring [74]. This might be attributed to the interaction of analyte gases to oxygen presented in the perovskite grain boundaries, which results in a fluctuation in electrical conductivity [75]. In this path, the majority of metal oxide perovskites were utilized towards the detection of various gaseous or hazardous volatile species [76–85]. In addition, numerous reviews and book chapters have explored and demonstrated these sensing applications in detail [86–90]. Therefore, the recently published sensory studies were mostly focused in this field.

Sensing responses of metal oxide perovskites are majorly attributed to the doping of ions or the composite mixture. Cao and coworkers reported the chlorine-doped nanocrystalline  $\text{LaFeO}_3$  powders towards ethanol gas sensing via resistance change [91]. They employed the citric sol–gel method to vary the chlorine doping in  $\text{LaFeO}_3$ , which enhanced the sensing performance via improved grain size and reduced intrinsic resistance. At 136 °C,  $\text{LaFeO}_{3-x}\text{Cl}_x$  ( $x = 0.6$ ) nanocrystalline demonstrated the better sensitivity to ethanol (200 ppm; ppm = parts per million) with the  $R_g/R_a$  response of 79.2 ( $R_a$  and  $R_g$  are resistance without and with the target gas). Upon exposure to ethanol gas, the electrons trapped by oxygen were released, hence an increase in resistance was observed as a sensor signal. This work was rather impressive in terms of the working temperature than that of few composite materials. For example, Zhang et al. reported ZnO nanoflowers decorated  $\text{LaMnO}_3$  nanoparticles for ethanol detection (50 ppm;  $R_g/R_a = 6.1$ ) operated at 300 °C [92]. Wherein, ZnO played a more vital role in the  $\text{LaMnO}_3@ZnO$  composite than  $\text{LaMnO}_3$ . However, analogous semiconducting nanocomposite metal oxide perovskites are still known as inspiring gas sensing materials [93] as detailed in Section 6.

Three diverse  $\text{PbTiO}_3$  nanostructures were hydrothermally synthesized from different  $\text{TiO}_2$  powders and utilized in gas sensing studies [94]. Nanoplate-like structures were demonstrated with better sensing performance to ethanol (5 ppm;  $R_g/R_a = 80.4$ ) via a change in resistance at 300 °C. Other analytes, such as xylene, acetone, toluene, HCHO, benzene,  $\text{NH}_3$ , CO and  $\text{NO}_2$  did not display significant selectivity. However, with the increased temperature to 500 °C, there was no selectivity to any gaseous species. Limit of detection (LOD) to ethanol by the  $\text{PbTiO}_3$  nanoplates was estimated as 88 ppb (ppb = parts per billion) in a wide range of humidity from 20 to 80%. This work was impressive, but the operation temperature still required to be reduced. Recently, Cao and coworkers proposed

using the Au and Cl co-modified LaFeO<sub>3</sub> nanoparticles (size = 29.5 nanometer (nm)) for the detection of ethanol gas (100 ppm;  $R_g/R_a = 220.7$ ) at 120 °C [95]. Au and Cl co-modified LaFeO<sub>3</sub> was synthesized by the sol–gel method and the sensor signal was attained via resistance change. They improved the ethanol sensing characteristics of Cl-doped LaFeO<sub>3</sub> [91] by the inclusion of the Au atom.

Growth of miscellaneous nanostructured metal oxide semiconducting perovskites to detect assorted gaseous species has recently attracted much attention. For instance, MA et al. synthesized the *p*-type PrFeO<sub>3</sub> (praseodymium ferrite) mesoporous hollow nanofibers through electrospinning and calcination procedures and employed in gaseous acetone discrimination [96]. When exposed to 200 ppm of various gases at 180 °C, PrFeO<sub>3</sub> nanofibers showed exceptional selectivity to acetone ( $R_g/R_a = 141.3$ ) with long term stability as shown in Figure 3. Oxygen in air was adsorbed on the surface of PrFeO<sub>3</sub> to capture the electrons of materials and increased the hole concentration, hence the resistance decreased. However, when the acetone gas entered, it interacted with chemisorbed oxygen and released the electrons to recombine with holes, which resulted in increased resistance (this mechanism is applicable to the majority of volatile organic compounds (VOCs)). Moreover, PrFeO<sub>3</sub> hollow nanofibers also displayed linear resistance change from 10 to 500 ppm acetone gas. Therefore, one can certainly endorse the potential acetone sensing ability of PrFeO<sub>3</sub> hollow nanofibers.

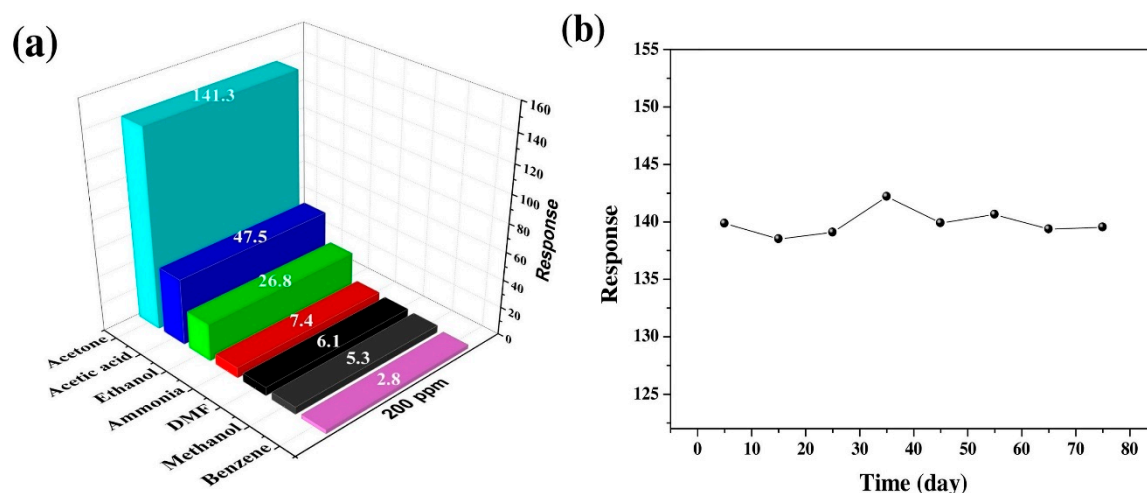


**Figure 3.** (a) The responses to different gases of 200 ppm at 180 °C and (b) the long-term stability of all the sensors to 200 ppm acetone at 180 °C (reproduced with the permission from reference [96]).

Acetone gas sensing was also achieved by Ag functionalized ZnSnO<sub>3</sub> nanocubes synthesized via solvothermal tactics [97]. At the 0.6% atomic ratio of Ag, the sensing response of ZnSnO<sub>3</sub> at 280 °C seems to be linear from 31.62 to 100 ppm with a LOD of 1 ppm. A 3.18 times higher response than pristine ZnSnO<sub>3</sub> was achieved using Ag functionalized ZnSnO<sub>3</sub> nanocubes in acetone gas sensing. This work is an impressive one in terms of the detection limits, but the operating temperature still requires further optimization. Through the sol–gel method, researchers fabricated the Pd-doped SmFe<sub>1-x</sub>Mg<sub>x</sub>O<sub>3</sub> ( $x = 0, 0.1, 0.2, \text{ and } 0.3$ ) nanocrystalline powder and La<sub>1-x</sub>Y<sub>x</sub>MnO<sub>3+ $\delta$</sub>  ( $x = 0 \text{ and } 0.15$ ) nanoparticles towards acetone gas detection [98,99]. Even though both materials demonstrated extensive responses, the operating temperatures (220 °C and 300 °C) still need to be reduced. To this direction, Au functionalized indium-doped ZnSnO<sub>3</sub> nanofibers were fabricated via electrospinning technique [100], which displayed sensitivity to 50 ppm acetone at 200 °C with a fast response/recovery time (10 s/13 s). As shown in Figure 4, the presence of Au and In<sup>3+</sup> in 0.25 Au/In-ZnSnO<sub>3</sub> could enhance the generation of electrons and hence a sensor response of this material was improved considerably. In addition, Au/In-ZnSnO<sub>3</sub> showed good stability in humid conditions via Au NPs-based inhibition of water vapor influence.

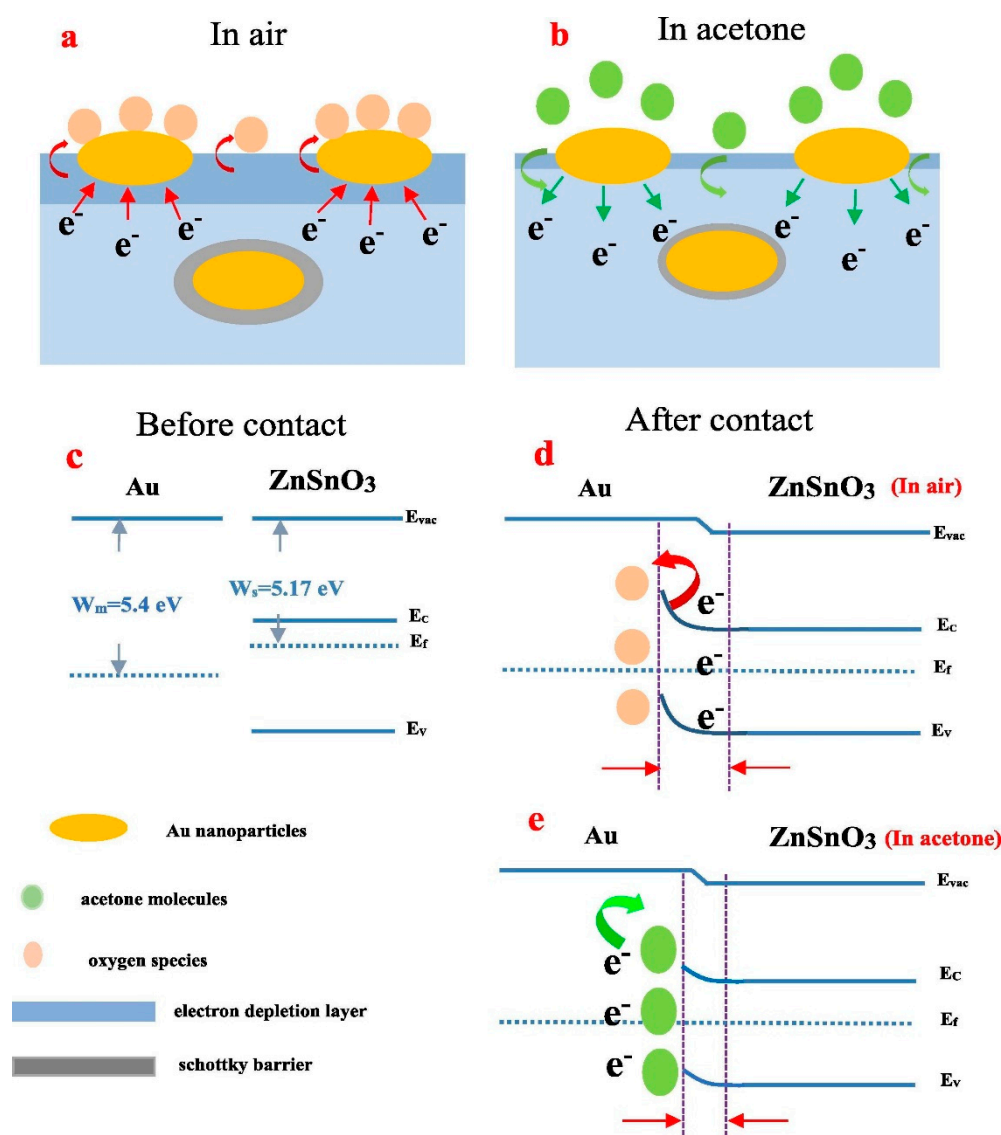
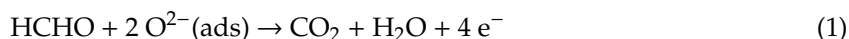


**Figure 4.** (a–e) Schematic illustration of the sensing mechanism of 0.25 Au/In-doped ZnSnO<sub>3</sub> sensor representing the Au enhanced electron generation in the presence of acetone (reproduced with the permission from reference [100]).

Subsequently, with the concern in volatile organic compounds (VOC) sensing, an xylene gas sensor was reported based on Ag-LaFeO<sub>3</sub> nanoparticles (40 and 60 nm) synthesized from the lotus leaf biotemplated sol–gel process [101]. This *p*-type sensor can operate at 125 °C with good humidity and long-term stability. Notably, it exhibits a high response ( $R_g/R_a = 16.76$ ) to 10 ppm of xylene gas with a fast response and recovery (68 s and 36 s). This is one of the best works towards xylene gas detection in terms of the functioning temperature. Similar to the earlier report [96], Ma and coworkers presented *p*-type samarium ferrite (SmFeO<sub>3</sub>) nanofibers towards effective detection of ethylene glycol at 5 ppm low concentration [102]. The response reached 18.19–100 ppm ethylene glycol with slightly higher operating temperature (240 °C), which required further investigation. Towards VOC discovery, Yin et al. recently described the *n*-propanol sensing using dense-packed *n*-type ZnSnO<sub>3</sub> nanospheres with approximately 500 nm in diameter prepared by coprecipitation method [103]. The sensor delivered a good response at 200 °C in high humid conditions. Response ( $R_g/R_a$ ) reached 17.7 at 50 ppm of *n*-propanol and the estimated LOD was 500 ppb ( $R_g/R_a = 1.7$ ). The above material can be consumed

towards the discrimination of *n*-propanol in the presence of other analytes, such as acetone, xylene, ammonia, methane and hydrogen.

Formaldehyde is a biotoxic VOC, hence researchers have developed the metal oxide perovskites for its recognition by the following mechanism.



The released electrons are trapped by the adsorbed oxygen, leading to the decrease in hole concentration and conductivity. Thereby, the sensor response is reflected in the resistance change. Ag-doped LaFeO<sub>3</sub> nanofibers were synthesized by the electrospinning method and employed in formaldehyde (HCHO) sensing studies [104]. As shown in Figure 5, upon exposure of 100 ppm of analytes (ammonia (NH<sub>3</sub>), toluene (C<sub>7</sub>H<sub>8</sub>), ethanol (C<sub>2</sub>H<sub>5</sub>OH), formaldehyde (HCHO), acetone (CH<sub>3</sub>COCH<sub>3</sub>) and xylene (C<sub>8</sub>H<sub>10</sub>)), Ag-LaFeO<sub>3</sub> nanofibers responded to the HCHO gas at 230 °C. This work still requires further optimization for optimum working temperature. To this approach, Yang et al. developed the porous LaFeO<sub>3</sub> via sol–gel and calcination techniques and utilized it in the HCHO sensing at 125 °C [105]. This material can detect 50 ppm with an R<sub>g</sub>/R<sub>a</sub> response of 116 and response/recovery time of 7/24 sec, hence attested as a decent work in formaldehyde identification.

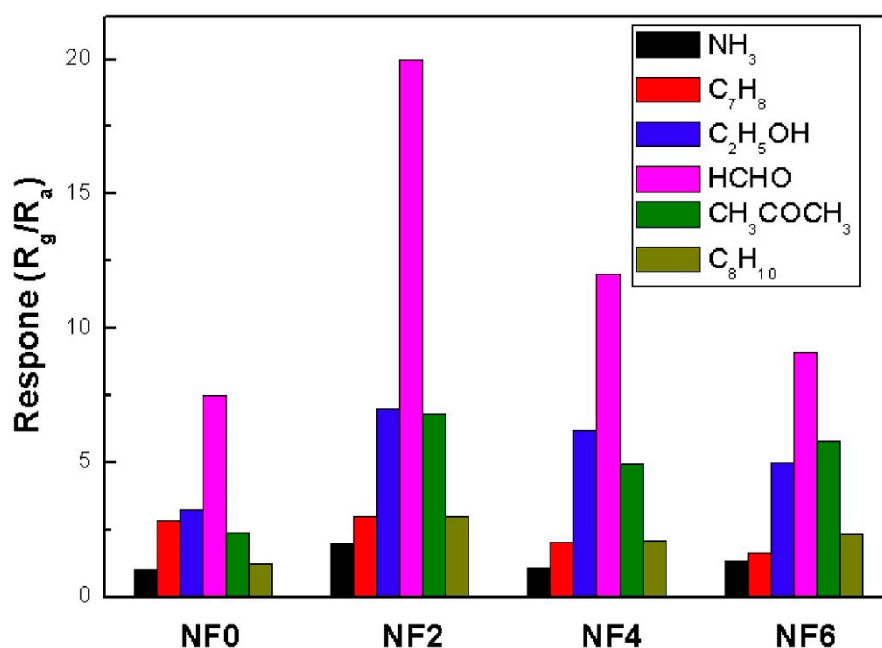
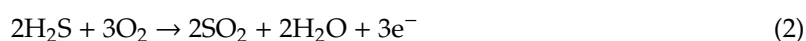


**Figure 5.** Responses of the sensors to 100 ppm different gases at their optimum working temperature; LaFeO<sub>3</sub> nanofibers doped by different amounts of Ag were marked as NF0, NF2, NF4 and NF6 (reproduced with the permission from reference [104]).

On the other hand, flammable/toxic gas detection was also explored by many metal perovskite nanostructures as discussed in the following. Flammable H<sub>2</sub> gas sensing by Ca-doped BiFeO<sub>3</sub> through the sol–gel method was proposed by Bala and coworkers [106]. At 15% Ca doping, BiFeO<sub>3</sub> showed a good sensor response (212% for 500 ppm H<sub>2</sub>) at 250 °C. Due to the incorporation of Ca<sup>2+</sup>, the oxygen vacancy concentration increased and hence achieved a good gas sensing property. In this way, toxic CO/CO<sub>2</sub>/propane gas discrimination by LaFeO<sub>3</sub>, LaCoO<sub>3</sub> and GdCoO<sub>3</sub> nanostructures with and without doping was reported with diverse responses and temperatures [107–111]. These nanostructures can be synthesized from solvent evaporation (through microwave irradiation) followed by calcination, the coprecipitation method and solution polymerization tactics. Moreover, by following a similar mechanism (as in VOCs recognition), they revealed exceptional responses to different gas concentrations at above 150 °C. The structural effect of gas sensing A<sub>2</sub>BB'O<sub>5</sub> (A = Ca, Sr; B = Fe; B' = Fe, Mn) oxygen

deficient perovskites to O<sub>2</sub>, CO and CO<sub>2</sub> was investigated by the Karki research group. In their work, a clear sensing mechanism was provided [112].

Towards toxic gas recognition, Dai and coworkers reported the palladium-doped perovskite oxide (La<sub>0.8</sub>Sr<sub>0.2</sub>Fe<sub>0.95</sub>Pd<sub>0.05</sub>O<sub>3- $\delta$</sub> ) electrolyte for impedance metric sensing of NO<sub>2</sub> gas [113]. In the presence of H<sub>2</sub>, NH<sub>3</sub>, CH<sub>4</sub> and CO<sub>2</sub>, the impedance metric response was detected for the NO<sub>2</sub> gas. However, the electrodes act as a sensor at high temperature (>650 °C), hence optimization in temperature is required. Modification or doping of LaFeO<sub>3</sub> with Ca and Sm by means of sol-gel and calcination tactics could form different nanostructured perovskites that can be employed in the detection of toxic SO<sub>2</sub> gas [114,115]. In contrast to the LaCaFeO<sub>3</sub> with operation temperature at 275 °C [114], LaSmFeO<sub>3</sub> [115] showed better performance with a LOD of 0.017 ppm at room temperature. Recently, Queralto et al. developed the LaFeO<sub>3</sub> nanofibers via calcination at 600 °C for the sensing of sulphur containing gases [116]. This *p*-type nanofibers possess a wide surface area and display a better reproducible chemoselectivity to SO<sub>2</sub> and H<sub>2</sub>S in the temperature range of 150–300 °C. The mechanistic aspect of the detection of H<sub>2</sub>S is noted in the Equation (2).



With the optimum LOD (4 ppm) and response/recovery time (60–360 s/180–500 s), LaFeO<sub>3</sub> nanofibers are the best material to be employed in the sulphur containing gas detection.

Similar to the toxic gas/VOC determination, metal oxide perovskites were also employed as humidity sensors. Sol-gel method mediated synthesis of magnesium- (Mg) or samarium- (Sm) doped nanocrystals of LaFeO<sub>3</sub> and LaMnO<sub>3</sub> perovskites were demonstrated in humid sensing applications [117,118]. LaMg<sub>x</sub>Fe<sub>1-x</sub>O<sub>3- $\delta$</sub>  (x = 0.0, 0.2, 0.4, 0.6, 0.8 and 1.0) responded to different humid conditions by the change in resistance. A similar response from the La<sub>0.7</sub>Sr<sub>0.3</sub>MnO<sub>3</sub> (LSMO) nanocrystals was detected through the impedance analyzer. LSMO nanocrystals showed a comparatively faster response (0.8 s) from 11% to 95% humidity (RH) at 10 Hz. Metal oxide nanoperovskites were also utilized in the electrochemical analyte determination as discussed next.

The non-enzymatic/enzymatic determination or direct recognition of analytes, such as glucose, *p*-phenylenediamine and H<sub>2</sub>O<sub>2</sub> has been demonstrated using modified metal oxide perovskite electrodes [119–122]. Atta group compared the non-enzymatic glucose detection by A and B site doping on strontium palladium perovskite (Sr<sub>2</sub>PdO<sub>3</sub>) with Ca<sup>2+</sup> and Au<sup>3+</sup> ions (among Ni<sup>2+</sup>, Cu<sup>2+</sup>, Au<sup>3+</sup> and Pt<sup>2+</sup>), respectively [119,121]. As shown in Figure 6, the amperometric response of graphite/Sr<sub>2</sub>Pd<sub>0.7</sub>Au<sub>0.3</sub>O<sub>3</sub> is much better than graphite/Sr<sub>2-x</sub>Ca<sub>x</sub>PdO<sub>3</sub> (x = 0–0.7) with LODs of 0.202 μM (micromole) and 2.11 nM (nanomole), correspondingly. This work can be used in the electrochemical catalytic estimation of glucose. Toxic *p*-phenylenediamine (PPD) in hair dyes was electrochemically detected by Sr-doped PrCoO<sub>3</sub> (Pr<sub>1-x</sub>Sr<sub>x</sub>CoO<sub>3- $\delta$</sub>  (x = 0, 0.2, 0.4, 0.6, 0.8 and 1)) modified glassy carbon electrodes (PSC82/GCE) in alkaline solution [120]. The electrode displayed highest responses of 655 and 308 μA mM<sup>-1</sup>cm<sup>-2</sup> in the PPD concentration range of 0.5–2.9 mM (millimole) and 2.9–10.4 mM, individually, with a LOD of 0.17 μM. However, this work still needs more effort to optimize the range of detection and LOD. Similarly, Y-doped (8% mol) SrTiO<sub>3</sub> displayed electrochemical sensitivity to H<sub>2</sub>O<sub>2</sub> with a LOD of 14.97 μM [122], which also requires further improvement.

Similar to device- and electrochemical-based analyte discovery, solution-mediated fluorescent sensing of nitramine explosives was also established by SmCrO<sub>3</sub> perovskite oxide (SCO) nanopowder [123]. SmCrO<sub>3</sub> nanopowder was synthesized by the sol-gel method (assisted by citric acid and cetyltrimethylammonium bromide (CTAB) in water) and employed in nitro explosives (TNP, TNT, HMX and RDX) detection in ethyl acetate (EtOAc), tetrahydrofuran (THF) and ethyl methyl ketone (EMK) at room temperature. As displayed in Figure 7, SCO shows better selectivity to nitro explosives than other competitive analytes and solvents. Moreover, it revealed a fast response to all explosives with LODs in the range of 6 × 10<sup>-8</sup> to 9.6 × 10<sup>-7</sup> M. Regarding the fluorescence-based sensing, this work is an exceptional example, thereby this tactic can be extensively used for other analytes.

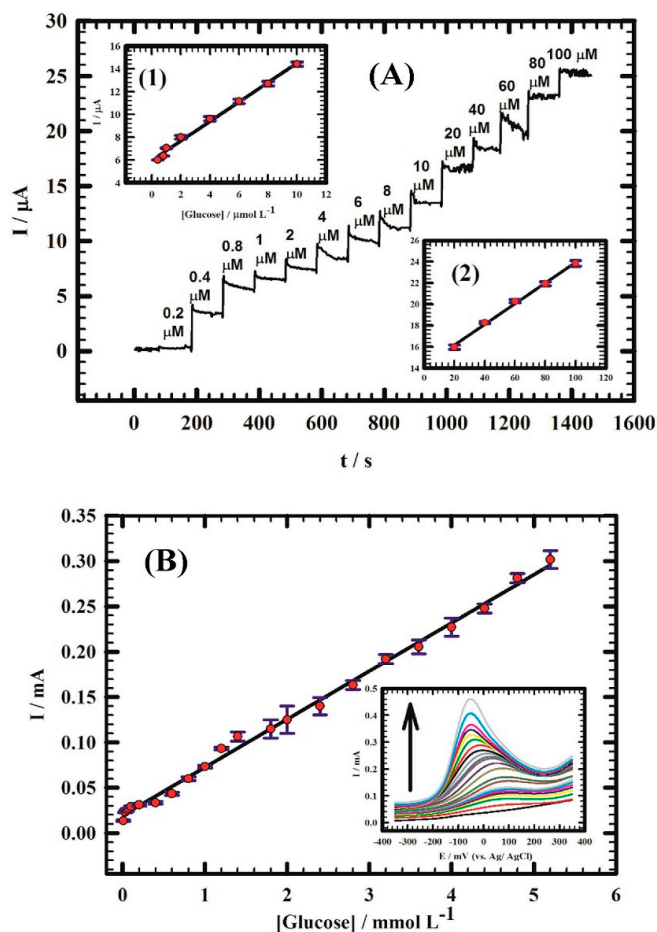


**Figure 6.** (A) Amperometric response of graphite/Sr<sub>2</sub>Pd<sub>0.7</sub>Au<sub>0.3</sub>O<sub>3</sub> with successive additions of glucose from 0.2 to 100  $\mu\text{M}$ . Insets (1, 2): calibration curves for glucose for concentrations from 0.4 to 10  $\mu\text{M}$  and from 20 to 100  $\mu\text{M}$ , respectively. We used 0.1 M NaOH and an applied potential of  $-76$  mV. (B) Calibration curve for glucose in diluted urine for concentrations from (10–5.2  $\mu\text{M}$ ). Inset: Linear sweep voltammetry (LSVs) of 10 mL of diluted urine at graphite/Sr<sub>2</sub>Pd<sub>0.7</sub>Au<sub>0.3</sub>O<sub>3</sub> in different concentrations of glucose (10–5.2 mM; reproduced with the permission from reference [121]).

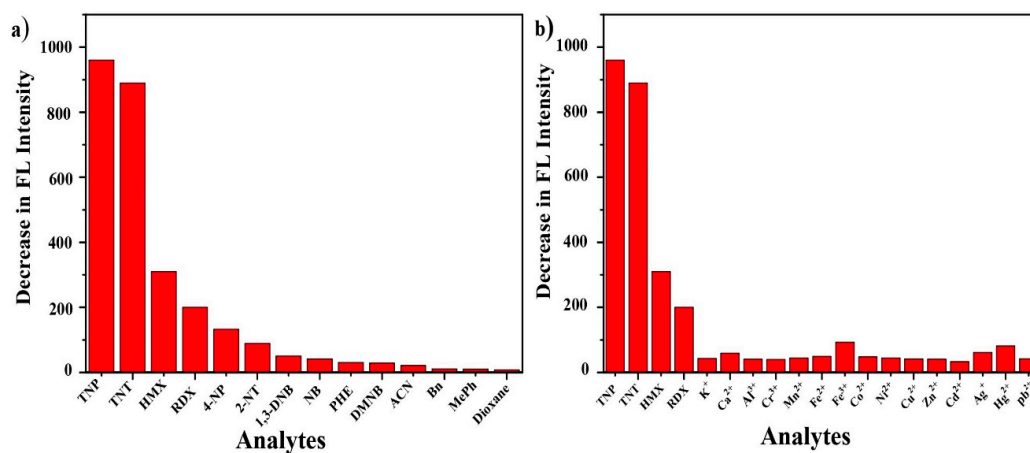


**Figure 7.** Graphs for selectivity test of SCO in the presence of the (a) nitro compound, aromatic and nonbenzene solvents and (b) various metal ions (the concentration of TNP, TNT, HMX, RDX and the materials used was 30  $\mu\text{M}$  in SCO (100 ppm); reproduced with the permission from reference [123]).

Next, Hernández-Rodríguez et al. described the Nd<sup>3+</sup>-doped (1.0% mol) yttrium orthoaluminate nanoperovskites (by the sol–gel method) for temperature sensing in the first and second biological windows (293–611 K), which can be employed in subtissue luminescence imaging [124]. Likewise, nanostructured *p*-type LaCoO<sub>3</sub> was synthesized by solution polymerization tactics and engaged in ultraviolet detection [125]. When exposed to a UV light source, the material showed changes in resistance. These results further confirm the exceptional analytical applications of metal oxide perovskites.

## 5. Metal Halide Perovskites in Analyte Detection

Recently, inorganic halide perovskites have been explored in many opto-electronic and photoelectrochemical studies [126]. Especially, rare earth metal containing halide perovskites were investigated for novel applications [127]. Their properties, like the instability in water or aqueous media, were established as aqueous sensors. For example, Aamir and coworkers proposed the cesium copper bromide (CsCuBr<sub>3</sub> by wet chemical method) perovskites for aqueous contamination detection by means of a PL “turn-on” response [128]. In parallel, lead-free zero-dimensional (0D) indium-based perovskite (Cs<sub>2</sub>InBr<sub>5</sub>·H<sub>2</sub>O) single crystal has been developed for water detection [129]. This material displayed a photoluminescence quantum yield (PLQY) of 33% in red emission with water sensing via a PL response.

Towards metal ions discrimination, inorganic halide perovskites were effectively employed with certain promising applications. For instance, Sheng et al. established the metal ions sensing ability of cesium lead halide perovskites quantum dots via detecting changes in fluorescence [130]. As shown in Figure 8, CsPbBr<sub>3</sub> quantum dots (QDs) revealed luminescence quenching in the presence of Cu<sup>2+</sup> ions but displayed enhancement with Yb<sup>3+</sup> ions. This halide perovskite probe was synthesized through hot-injection tactic with PLQY of 63%. It demonstrated exceptional linear responses ( $2 \times 10^{-9}$  to  $2 \times 10^{-6}$  M) when applied on Cu<sup>2+</sup> sensing in edible oils. Similarly, CsPbBr<sub>3</sub> perovskite quantum dots (PQDs) were also reported by Liu and coworkers for Cu<sup>2+</sup> quantification with a linear range of 0–100 nM and LOD of 0.1 nM [131]. From both work, it was concluded that luminescent CsPbBr<sub>3</sub> is a good material for the PL-based Cu<sup>2+</sup> sensing.

PL tuned sensing of Cu<sup>2+</sup> ions was also demonstrated by europium (Eu<sup>3+</sup>)-doped lead free Cs<sub>3</sub>Bi<sub>2</sub>Br<sub>9</sub> perovskite quantum dots [132]. The Eu<sup>3+</sup> incorporated Cs<sub>3</sub>Bi<sub>2</sub>Br<sub>9</sub> QDs with PLQY of 42.4% were prepared from the ligand assisted reprecipitation method and applied in PL based Cu<sup>2+</sup> sensor. Linear range of Cu<sup>2+</sup> detection was found to be 5 nM to 3 μM with a LOD of 10 nM, which enabled feasible extension of such QDs in metal ions quantification. Recently, CsPbBr<sub>3</sub> QDs facilitated ultra-trace sensing of uranyl ions (UO<sub>2</sub><sup>2+</sup>) has been reported by Halali and coworkers [133]. Through hot-injection method, CsPbBr<sub>3</sub> QDs were synthesized. The PL intensity was significantly quenched (LOD = 83.33 nM) only when UO<sub>2</sub><sup>2+</sup> ions (from 0 nM to 3.3 μM) were added into the solution, as displayed in Figure 9. This probe follows the adsorption mechanism and allows the researchers to extend their trend towards the assay of a nuclear hazard.

Related to the metal ions assay, Cs comprising of nano perovskites were also used in diverse recognition studies. Lead free Cs<sub>2</sub>BiAgBr<sub>6</sub> double perovskites have been applied in humidity (5–75%) sensing with a superfast response and recovery time (0.45 s/1.78 s) [134]. Fabrication of Cs<sub>2</sub>BiAgBr<sub>6</sub> was carried out by spin coating. It can detect changes in humidity with a linear range of 15–78%. Subsequently, Chen et al. reported the medically important gas sensing property of nanostructured and light-activated CsPbBr<sub>2</sub>I (CPBI) perovskite, which can detect the reducing (e.g., acetone and propane) and oxidizing (e.g., NO<sub>2</sub> and O<sub>2</sub>) gas molecules with limits down to 1 ppm [135]. However, due to its non-specificity, this work can be considered as an addition to the device-based gas sensor. In general, Cs incorporated inorganic halide perovskites (particularly the CsPbX<sub>3</sub> (X = Cl, Br and I) nanostructures) display high luminescence properties upon light activation [136]. This property allows the scientist to explore their innovative and analytical applications. Research groups employed the porous network of nanostructured CsPbBr<sub>3</sub> (CPB) in the recognition of ethanol and acetone via O<sub>2</sub> (generated from

solvents) mediated surface passivation and ambipolar charge transport in the perovskite layer [137]. The probe can detect the VOCs down to 1 ppm at room temperature with excellent response and recovery time.

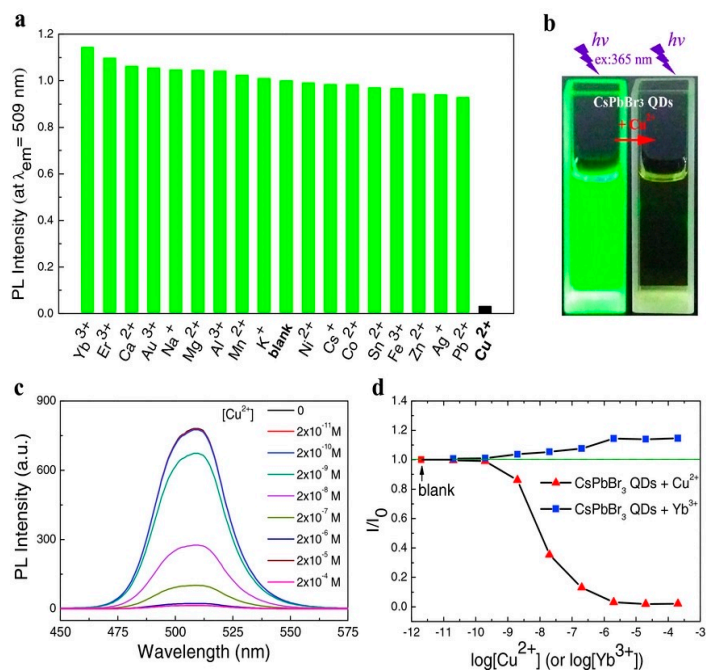


**Figure 8.** (a) The effect of different metal ions on the PL intensity of the CsPbBr<sub>3</sub> QDs. The concentration of metal ions and the CsPbBr<sub>3</sub> QDs are  $2.0 \times 10^{-6}$  and  $\approx 1.0 \times 10^{-9}$  M, respectively. The PL peak intensity is normalized by the CsPbBr<sub>3</sub> QDs without addition of metal ions (the “blank” column); (b) images of the CsPbBr<sub>3</sub> QDs in cyclohexane under ultraviolet light excitation with and without Cu<sup>2+</sup>; (c) the [Cu<sup>2+</sup>] on PL spectrum of the CsPbBr<sub>3</sub> QDs and (d) the [Cu<sup>2+</sup>] and [Yb<sup>3+</sup>] on PL intensity of the CsPbBr<sub>3</sub> QDs ( $\lambda_{ex} = 365$  nm; reproduced with the permission from reference [130]).

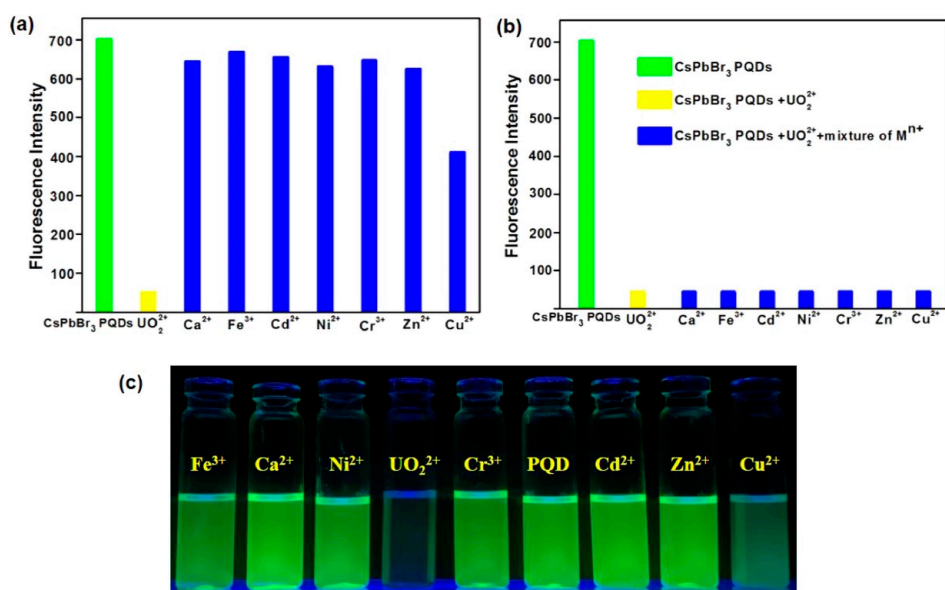


**Figure 9.** (a) Change in the PL of CsPbBr<sub>3</sub> PQDs upon the addition of various ions. (b) Effect of interfering cations with the absorption of bare CsPbBr<sub>3</sub> PQDs and CsPbBr<sub>3</sub> PQDs + UO<sub>2</sub><sup>2+</sup> complex (c) Digital photograph of colorimetric changes of the probe upon addition of various metal ions (reproduced with the permission from reference [133]).

Luminescence property of CsPbBr<sub>3</sub> nanocrystals plays a more vital role in the detection of HCl gas than other analytes (such as HNO<sub>3</sub>, CH<sub>3</sub>COOH, HBr, NH<sub>4</sub>OH, H<sub>2</sub>O and HCOOH) by means of an anion exchange reaction to form CsPb(Br/Cl)<sub>3</sub> [138]. The probe was synthesized by a routine hot-injection procedure to detect HCl gas with a LOD down to 5 ppm, thereby can be extended for real time monitoring. In this light, Chen and coworkers used the fluorescent CsPbBr<sub>3</sub> quantum dots for rapid H<sub>2</sub>S determination in rat brain microdialysis [139]. Upon the addition of H<sub>2</sub>S, luminescence of CsPbBr<sub>3</sub> QDs was quenched linearly from 1 to 100 μM with a LOD of 0.18 μM. This work is an impressive one with a rat brain based H<sub>2</sub>S assay. Exploration of CsPbBr<sub>3</sub> QDs-based ammonia gas sensing was delivered by the Huang research group [140]. As shown in Figure 10, CsPbBr<sub>3</sub> QDs show a turn-on resistance change to ammonia from 25 to 350 ppm (LOD = 8.85 ppm) with response/recovery time of 10/30 s, correspondingly. This report was an inspiring addition to ammonia sensors.

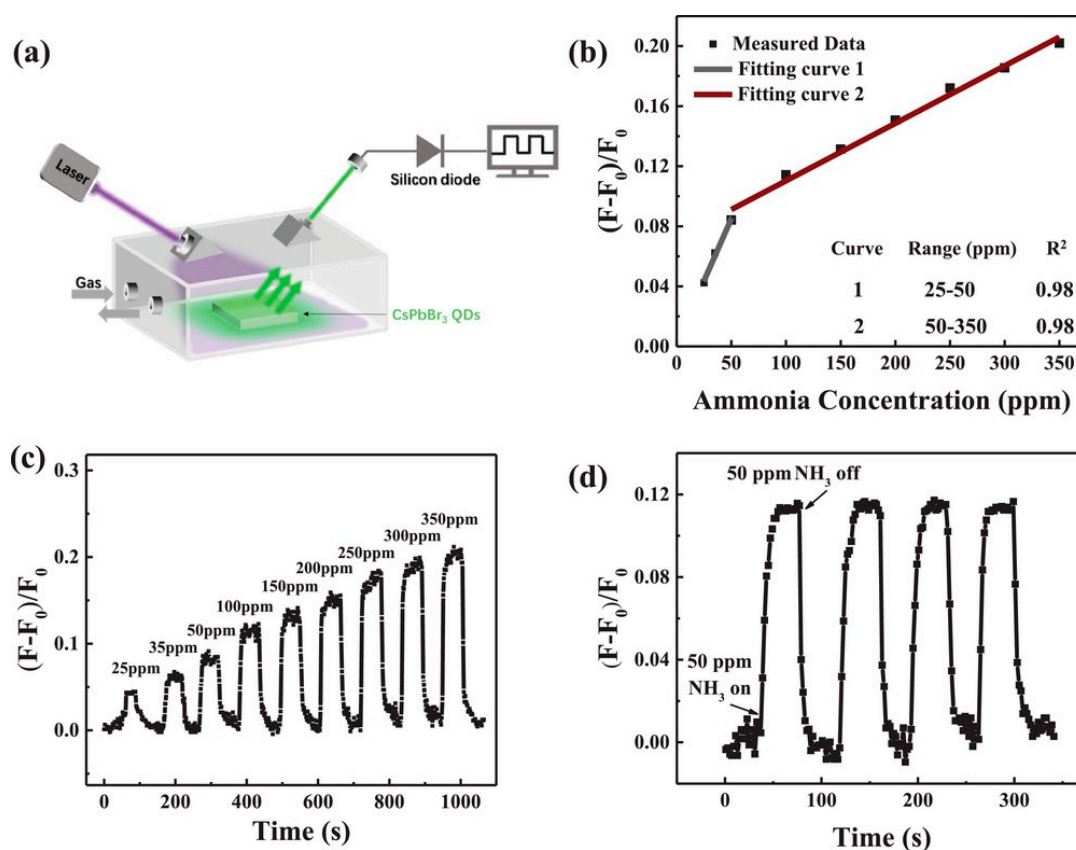


**Figure 10.** (a) Experimental setup for characterization. A fiber is on the right side to the transmission excitation light (365 nm), the pipeline for controlling ammonia flow is on the left side and (b) a fitting curve for the sensing response value of PL intensity. The inset is the fitting parameters of the two fitting curves; (c) dynamic sensing responses of different NH<sub>3</sub> concentrations (from 25 to 350 ppm) and (d) four successive sensing cycles of the CsPbBr<sub>3</sub> QDs sensor (50 ppm; reproduced with the permission from reference [140]).

In recent times CsPbX<sub>3</sub> (Br/I) nanostructures were employed in the identification of ozone (O<sub>3</sub>) and explosive picric acid [141,142]. The fabricated film composed of CsPbBr<sub>3</sub> nanocubes displayed high sensitivity to O<sub>3</sub> environment at room temperature [141]. Before the exposure to O<sub>3</sub>, the nanocubes adsorbed the O<sub>2</sub> species and became resistive with less conductive holes. This phenomenon was completely reversed upon exposure to O<sub>3</sub> (act as electron acceptor), as shown in Figure 11, where the conductive holes concentration was enhanced and an increase in the current response was observed. This work has pointed to the exceptional direction in inorganic metal halide perovskite-based sensor research. Next, as illustrated in Figure 12, CsPbBr<sub>3</sub> PQDs and CsPbI<sub>3</sub> PQDs (prepared by the

hot-injection method with PLQY = 52.88% and 46.18%,) display PL quenching to picric acid in solution with estimated LODs of 0.8 nM and 1.9 nM, respectively [142]. In the presence of other competing analytes like 2,4,6-trinitrotoluene (TNT), 2,4-dinitrotoluene (DNT), nitrobenzene (NB), benzoic acid (BA), 1,3-dinitrobenzene (DNB) and benzaldehyde (BD), PQDs showed exceptional selectivity to picric acid with inkjet printing applications, thereby they attested as a nice report in the explosive sensor.

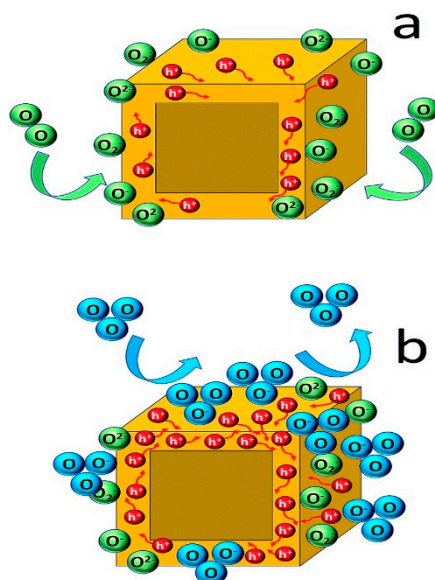


**Figure 11.** Schematic diagram of the gas sensing mechanism under ambient conditions (a) and after ozone exposure (b) (reproduced with the permission from reference [141]).

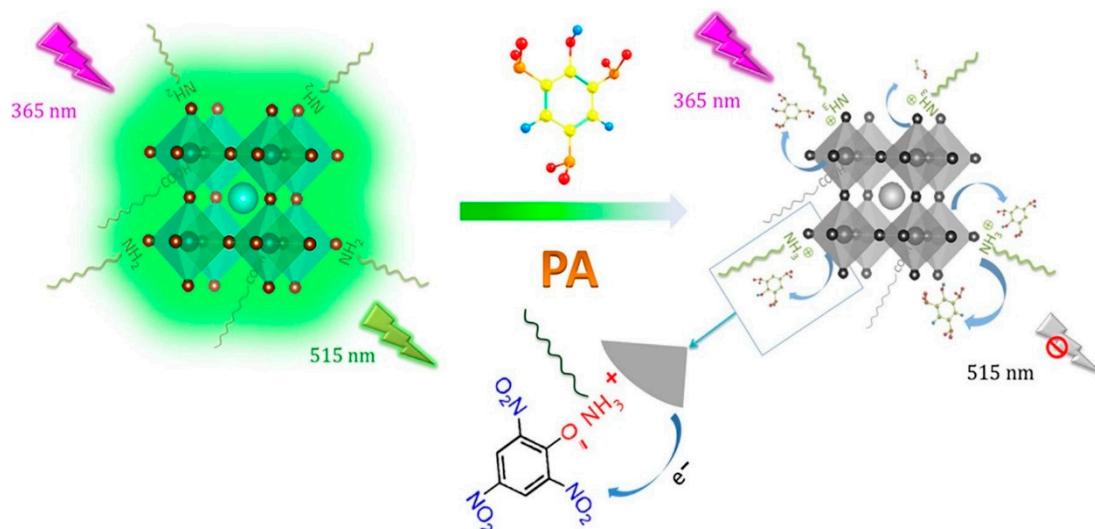


**Figure 12.** Schematic illustration for the sensitive fluorescence detection of picric acid (PA) -based on perovskite quantum dots (reproduced with the permission from reference [142]).

Similar to inorganic halide, organometal halide perovskites also become effective in sensory research due to their unique fluorescence and solvent tuned aggregation induced emission (AIE) characteristics [143]. Earlier, Muthu et al. denoted the organic–inorganic perovskite ( $\text{CH}_3\text{NH}_3\text{PbBr}_3$ ) nanoparticles (6.1 nm size) for the luminescent detection of picric acid [144]. As represented in Figure 13, upon the addition of picric acid (TNP), 97% of PL quenching was attained with LOD down to femtomolar ( $1 \times 10^{15}$  M). This is one of the pioneer works that have initiated the sensing applications of organometal halide perovskites. In contrary to the metal oxides, organometal halide perovskites

have been utilized in luminescent- and device-based humidity sensors [145–147]. A red emitting dye 5,10,15,20-tetrakis(pentafluorophenyl)porphyrin was coupled with  $\text{CH}_3\text{NH}_3\text{PbBr}_3$  nanocrystalline perovskite film, which revealed reversible sensitivity to humidity between the range of 7–98% via green to red color change and fluorescent quenching [145]. This sensor response is visible to the naked eye with a LOD of 0.04% RH, thereby attested as exciting research.

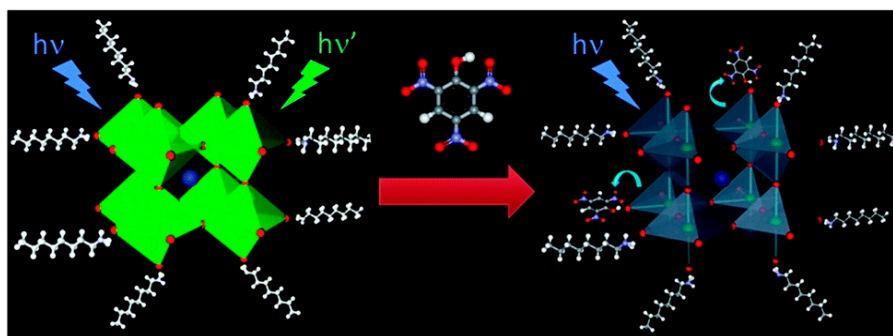


**Figure 13.** Schematic illustration for the sensitive fluorescence detection of PA based on perovskite quantum dots (reproduced with the permission from reference [144]).

Toward humidity sensing, Ren et al. fabricated the  $\text{CH}_3\text{NH}_3\text{PbI}_{3-x}\text{Cl}_x$  ( $x = 0, 2.8$ ) nanosheet arrays that responded to humidity change in their resistance [146]. Herein, from low humidity (30% RH) to 90% RH at 27 °C, the resistance fluctuated from  $1.28 \times 10^8$  to  $7.39 \times 10^4 \Omega$ . The sensor performance was far better than the commercial psychrometer, thereby attested as a nice innovation. Recently, Gao and coworkers reported the luminescent chromism of nanocrystalline  $\text{PEA}_2\text{MnBr}_4$  (PEA = phenethyl-ammonium) single crystals observed through green to pink emission for humidity/moisture [147]. The LOD of the water content in toluene by this probe ranged between 0.02 and 0.05 vol %. However, this work needs further optimization to improve the humidity recognition. Apart from explosive and humidity quantitation, organometal halide perovskites were also employed in the sensing of cations, anions, toxic gases and VOCs as described in the following sections.

Tian research group demonstrated the  $\text{Hg}^{2+}$  ions detection by surface adsorbed fluorescent quenching of  $\text{CH}_3\text{NH}_3\text{PbBr}_3$  QDs (synthesized by ligand-assisted reprecipitation (LARP) technique with PLQY = 50.28%) [148]. As illustrated in Figure 14, the green fluorescence of QDs was linearly quenched with a LOD of 0.124 nM between the concentration ranges of 0–100 nM. They demonstrated the applicability in spot plate, which assured the proficiency of  $\text{CH}_3\text{NH}_3\text{PbBr}_3$  QDs in the  $\text{Hg}^{2+}$  assay. In this course,  $\text{Cu}^{2+}$  sensing has been validated by two-dimensional (2D)  $\text{PEA}_2\text{PbI}_4$  nanocrystals (PNCs) in water [149]. In which, the PL was quenched upon addition of  $\text{Cu}^{2+}$  ions from 0.5 nM to 50 mM. However, this work still requires extensive interrogation.

Similar to surface mediated cation discrimination, anion substitution could lead to opto-electronic/dimensional property alteration [150], hence perovskite facilitated anion sensory also attracted attention from researchers. For instance, Lu et al. established the fluoride sensing ability of dual ligands capped  $\text{CH}_3\text{NH}_3\text{PbBr}_3$  QDs (synthesized from LARP procedure with PLQY = 27.2%) through H-bonding between the fluoride anion and one of the capping ligand 6-amino-1-hexanol (AH) [151]. The QDs show better selectivity to  $\text{F}^-$  ions with negligible interference of other analytes as shown in Figure 15. A linear response to  $\text{F}^-$  was observed from 10 to 50  $\mu\text{M}$  with a LOD of 3.2  $\mu\text{M}$ . Until now, this work is still well recognized in the research of organometal halide based luminescent anion recognition.

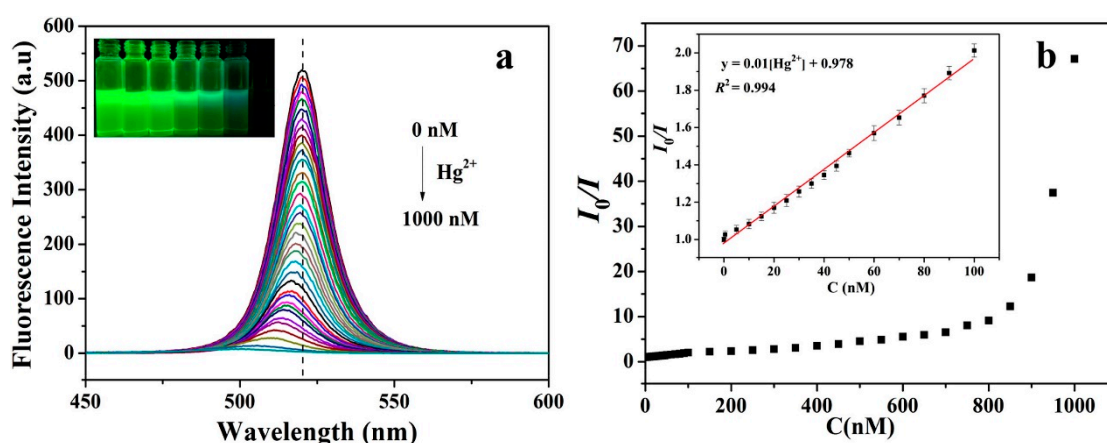


**Figure 14.** (a) Evolution of fluorescence spectra changes of  $\text{CH}_3\text{NH}_3\text{PbBr}_3$  QDs upon the addition of different amounts of  $\text{Hg}^{2+}$ . The concentration of  $\text{Hg}^{2+}$  from top to bottom: 0–1000 nM. (b) Linear fitting curve of  $I_0/I$  with respect to  $\text{Hg}^{2+}$  concentration over the range of 0–100 nM (reproduced with the permission from reference [148]).

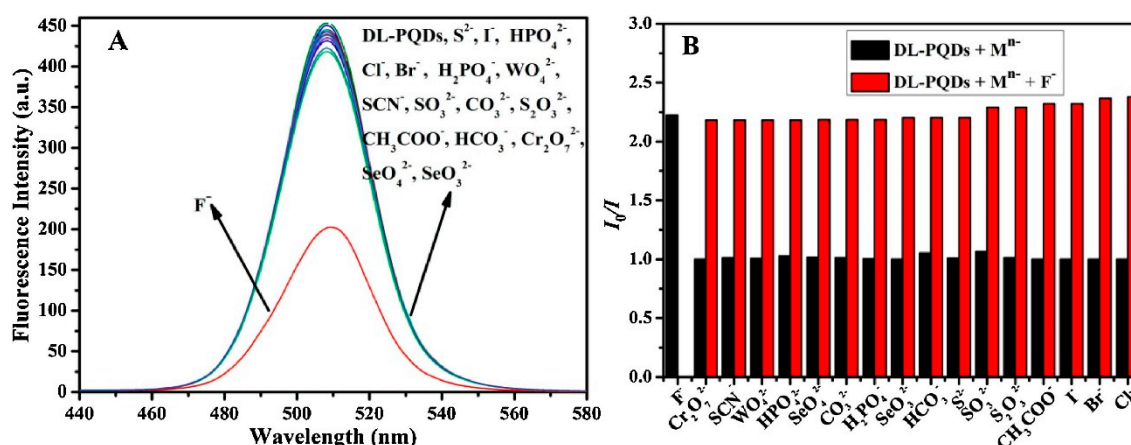


**Figure 15.** (A) Fluorescence response of dual ligand capped perovskite quantum dots (DL-PQDs) to different anions and  $\text{F}^-$  (90  $\mu\text{M}$  for  $\text{F}^-$  and 450  $\mu\text{M}$  for other anions). (B) Interference studies of the novel nanosensor toward  $\text{F}^-$ . The black bars represent the fluorescence response of DL-PQDs to  $\text{F}^-$  and other anions (90  $\mu\text{M}$  for  $\text{F}^-$ , 450  $\mu\text{M}$  for other anions). The red bars represent the change of emission occurred after the subsequent addition of 90  $\mu\text{M}$  of  $\text{F}^-$  to the above solutions (reproduced with the permission from reference [151]).

Organometal halide nanostructured perovskites were effectively used in the discrimination of VOCs by means of PL and resistance fluctuations [152–155]. Structural conversion through irreversible/reversible H-bonding in the perovskite-based aliphatic amines was proposed by Kim and coworkers [152]. Upon exposure to gaseous monoethylamine (competitor: diethylamine and trimethylamine), the green fluorescence of  $\text{CH}_3\text{NH}_3\text{PbBr}_3$  perovskite nanoparticles displayed 89% quenching within a second. However, this interrogation needs to be upgraded with many competing amines. In a similar fashion, a zero dimensional (0D) lead free  $(\text{C}_9\text{NH}_{20})_2\text{MnBr}_4$  ( $\text{C}_9\text{NH}_{20}^+ = 1\text{-butyl-1-methylpyrrolidinium cation}$ ) nanoperoovskite was employed in the sensing of acetone [153]. The material was synthesized from the wet-chemical route (PLQY = 81.08%). The green luminescence was quenched (50 fold) within 10 s upon exposure to acetone vapor.

Subsequently, a two dimensional (2D)  $(\text{C}_4\text{H}_9\text{NH}_3)_2\text{PbI}_2\text{Br}_2$  ( $\text{C}_4\text{H}_9\text{NH}_3^+ = n\text{-butyl ammonium ion}$ ) nanoperoovskite was synthesized by a wet-chemical procedure and employed in ppt (ppt = parts per trillion) level detection of benzene by means of a change in resistance [154]. The sensor

displays better response to benzene ( $R_g/R_a = 90.7$ ) at 160 °C with a LOD of 1 ppt than that of other analytes, such as toluene, ethanol, ortho-xylene and para-xylene gases. The report demonstrated an impressive LOD, but temperature needs to be optimized before commercialization. In this framework, the methylammonium lead iodide (MAPbI<sub>3</sub>) nanostructured perovskite thin film has been proposed to sense ethanol gas at room temperature [155]. Both the resistance and PL responses can be used for the determination of ethanol. However, the LOD of this ethanol sensor is approximately 1300 ppm, which require further improvement in perovskite-based sensing of VOCs.

Similar to the VOCs sensing, perovskites can be an exceptional candidate in toxic gas discrimination. Methylammonium lead tri-iodide (MAPbI<sub>3</sub>) hybrid perovskites display its high sensitivity to ammonia (NH<sub>3</sub>) gas through the resistance changes [156–158]. These reports involved the MAPbI<sub>3</sub> in the form of film, paper and powder pellet for NH<sub>3</sub> sensing with detectivity down to 1 ppm. Thus, the NH<sub>3</sub> recognition ability of MAPbI<sub>3</sub> is well established. Moreover, Jiao et al. reported the use of MAPbBr<sub>3-x</sub>I<sub>x</sub> in NH<sub>3</sub> detection, which work at 15 °C with high response values ( $R_g/R_a = 29.7$ ; 500 ppm) [159]. The material was synthesized via the one step spinning method. It displayed the detectivity of NH<sub>3</sub> gas down to 200 ppm and response-recovery time in less than 20 s due to acceleration of irreversible decomposition. Recently, Li and coworkers proposed the encapsulation tactics for PL-based assays of NH<sub>3</sub> gas [160]. In which, the MAPbBr<sub>3</sub> encapsulated by tetrabutylammonium cations (nano-MAPbBr<sub>3</sub>-TBA film) displayed linear PL quenching upon exposure to ammonia gas as illustrated in Figure 16. This NH<sub>3</sub> probe is effective in wide humid conditions with estimated LOD of 0.46 ppm. In the future, it can be used in ammonia detection with certain authorization. These organometal halide perovskites are currently more effective in various toxic gas sensing because of diverse quantum dynamics and surface properties [161].

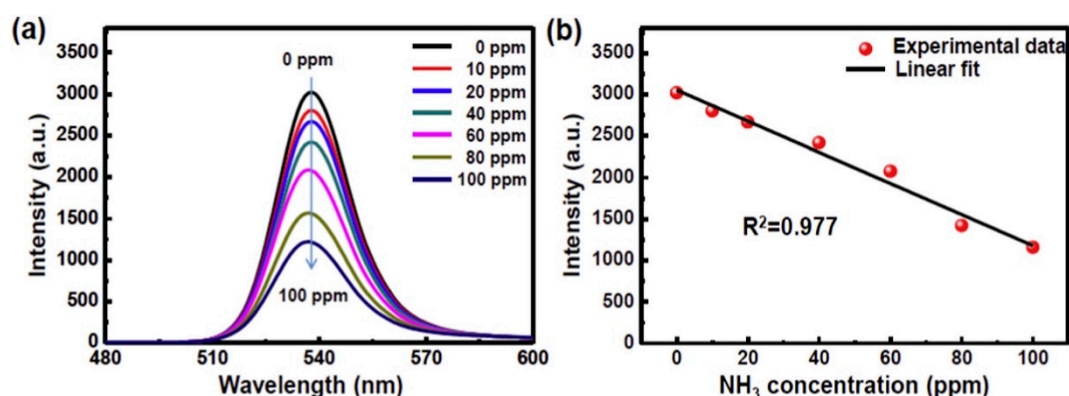


**Figure 16.** MAPbBr<sub>3</sub>-TBA-based gas sensor. (a) The PL quenching toward different concentration of gaseous NH<sub>3</sub> (0–100 ppm) and (b) the plot of PL intensity versus concentration of NH<sub>3</sub> (reproduced with the permission from reference [160]).

Nanostructured organometal halide perovskites were also utilized in the device-based assay of toxic NO<sub>2</sub> gas [162–166]. Thin film made of CH<sub>3</sub>NH<sub>3</sub>PbI<sub>3-x</sub>(SCN)<sub>x</sub>, CH<sub>3</sub>NH<sub>3</sub>PbI<sub>3</sub>, CH<sub>3</sub>NH<sub>3</sub>PbBr<sub>3</sub> and CH<sub>3</sub>NH<sub>3</sub>SnI<sub>3</sub> showed high selectivity to NO<sub>2</sub> with LODs of 200 ppb, 1 ppm, 1 ppm and 25 ppb, respectively, via resistance changes [162–165]. Moreover, CH<sub>3</sub>NH<sub>3</sub>PbI<sub>3-x</sub>(SCN)<sub>x</sub> also displayed its sensing ability to gaseous acetone with a LOD of 20 ppm. The underlying mechanism is that the NO<sub>2</sub> gas physically adsorbed on the surface of those films generates electrons from the conduction band or from charge transfer chemisorption. A triple cation containing FA<sub>0.80</sub>MA<sub>0.15</sub>Cs<sub>0.05</sub>PbI<sub>2.55</sub>Br<sub>0.45</sub> (FMCPIB) nanocrystalline perovskite was applied in the device-based detection of NO<sub>2</sub> gas by Chen and coworkers [166]. As shown in Figure 17, FMCPIB devices in the self- and externally-powered mode were able to detect NO<sub>2</sub> gas at room temperature with an estimated LOD of 0.2 ppm. This material is a unique one to be applied in NO<sub>2</sub> discrimination in the presence of competing species with a recover/response time of 17/126 s.

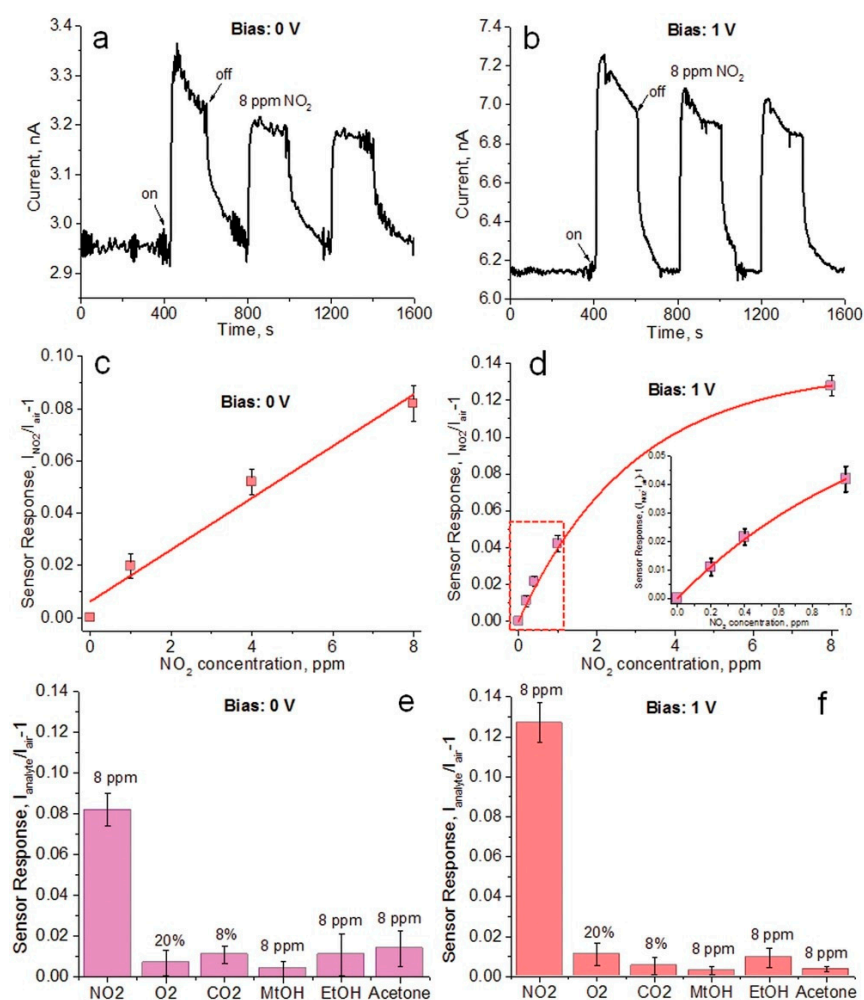


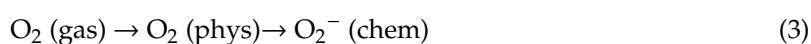
**Figure 17.** Room-temperature chemical response of the FMCPiB devices in the self- and externally-powered mode. Dynamic sensor response of an FMCPiB device to three consecutive injection of 8 ppm NO<sub>2</sub> (a) self-powered under weak fluorescent lamp light irradiation ( $1.3 \mu\text{W cm}^{-2}$ ) and (b) externally powered with 1 V bias in the dark. FMCPiB sensor response as a function of the NO<sub>2</sub> concentration; (c) in the self-powered mode and (d) at the 1 V external bias; the inset in (d) is the enlarged part of the red dashed region. The sensor response of the FMCPiB sensor for six different gases (e) in the self-powered operational mode; and (f) at the 1 V external bias. The gas sensing measurements were conducted at room temperature ( $30 \text{ }^\circ\text{C}$ ) under simulated air ( $V_{\text{N}_2}/V_{\text{O}_2} = 4$ ) with a constant total gas flow of  $0.5 \text{ L min}^{-1}$  (reproduced with the permission from reference [166]).

Organometal halide nanoperovskites were engaged in recognition of O<sub>2</sub>, O<sub>3</sub> and H<sub>2</sub> gases, as well as photo sensors [167–170] through conductivity responses. For example, Stoeckel et al. used the CH<sub>3</sub>NH<sub>3</sub>PbI<sub>3</sub> nanocrystalline film to determine O<sub>2</sub> concentration via the trap healing mechanism instigating from an O<sub>2</sub> tuned iodine vacancies filling with a detection limit down to 70 ppm [167]. This is an inspiring work on device-based O<sub>2</sub> detection at ambient conditions. Subsequently, the Petridis research group reported the O<sub>3</sub> and H<sub>2</sub> sensing by CH<sub>3</sub>NH<sub>3</sub>PbI<sub>3-x</sub>Cl<sub>x</sub> through electrical measurements [168,169] with slight variation in fabrication tactics. However, the responses of this sensor material in the presence of both gases (O<sub>3</sub> and H<sub>2</sub>) need to be established for validation. Next, the CH<sub>3</sub>NH<sub>3</sub>PbI<sub>3</sub> nanocrystalline film was grown by the pulsed laser deposition (PLD) process, which acted as a photo sensor over wavelengths from 375 to 800 nm at 5 V bias [170]. This material also exhibited a power conversion efficiency (PCE) of 10.6% and became a potential candidate in photonics research.

Apart from the sensing ability of organometal halide perovskites to VOCs, metal ions, anions, toxic gases and explosives, they can be used in electromechanical sensors. In this framework, Xia et al. reported the two dimensional (2D)  $(C_4H_9NH_3)_2PbBr_4$  as strain sensors, which displayed high sensitivity at a strain ratio of 0.16% with reversible stretchability [171]. This work is noted as an essential breakthrough in wearable sensor research. By combining with certain materials, these organic/inorganic metal halide perovskites may form nanocomposite like structures, which can be utilized in exceptional sensors like tactile sensors [172,173]. For instance, the nanocomposite like structure with a combination of ZnO nanosheet arrays and polystyrene (or  $CH_3NH_3PbI_3$  (MAPbI<sub>3</sub>)) acts as exceptional tactile sensors (with respective sensitivity of  $0.57 \text{ kPa}^{-1}$  and  $0.64 \text{ kPa}^{-1}$ ). The sensing applications of nanocomposites with perovskites are discussed in the next section.

## 6. Perovskites Incorporated Nanocomposites as Sensors

Metal oxide perovskites incorporated nanocomposites displayed high sensitivity to ethanol gas with exceptional response and recovery [92,174–176]. Wherein,  $LaMnO_3/SnO_2$  composite nanofibers [174] and  $\alpha\text{-Fe}_2O_3/LaFeO_3$  composite nanomaterial [175] delivered their sensitivity to 100 ppm ethanol at high operating temperatures 260 and 240 °C with responses of 20 and 10, respectively. In contrast, Chen et al. reported the  $Ag/Zn\text{-}LaFeO_3$  (AZLFO) nanocomposite-based ethanol detection, which showed a response of 64.2–100 ppm analyte and a detection limit down to 5 ppm [176]. Note that this sensor can operate from 55 to 245 °C. By following the reaction steps shown in Equations (3)–(5), ethanol sensing can be achieved near room temperature.



It has been established that the gas sensitivity is achieved due to fluctuations in electrical conductivity induced by surface chemisorbed oxygen species over the sensing materials. However, the Zn doping also plays a vital role for near room temperature sensing of ethanol. As illustrated in Figure 18,  $Zn^{2+}$  doping compensates the defects of La sites and increases the hole concentration, thus a higher sensor response is achieved near room temperature.

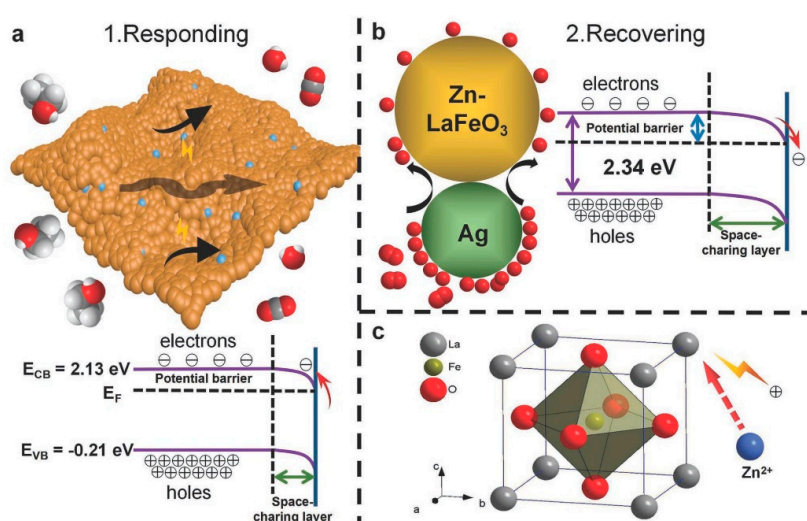


**Figure 18.** Schematic illustration of the sensing mechanism of the AZLFO-based sensors to ethanol: (a) exposed to ethanol; (b) exposed to air and (c)  $Zn^{2+}$  doping in the lattice of LFO (reproduced with the permission from reference [176]).

Such a composite structure has been applied in the sensing of gaseous acetone [177]. Three dimensional (3D)  $\text{LaFeO}_3/\alpha\text{-Fe}_2\text{O}_3$  nano-octahedrons were synthesized by the one-step solvothermal method, which were then combined with a metal–organic framework. The nano-octahedrons constructed heterostructures detect the acetone and obtain the sensor response ( $R_a/R_g = 21$ ) by means of changes in conductivity. The sensor can detect 100 ppm of acetone at 230 °C, thereby further optimization is required to reduce the working temperature. Porous  $\text{SnO}_2$  fiber-in-tubes (FITs) were functionalized with  $\text{La}_{0.75}\text{Sr}_{0.25}\text{Cr}_{0.5}\text{Mn}_{0.5}\text{O}_{3-\square}$  (LSCM) nanoparticles (215.7 nm in size; synthesized from the combustion method using citric acid) and employed in formaldehyde recognition [178]. The material (LSCM@ $\text{SnO}_2$  FITs) showed a high response to formaldehyde ( $R_a/R_g = 26.50$  at 5 ppm, 400 °C) with a LOD of 80 ppb. The above report is impressive work but the operation temperature must be reduced for practical applications. Later, hydrothermally synthesized nanoflowers like the  $\text{ZnSnO}_3/\text{Zn}_2\text{SnO}_4$  composite hybrid has been reported for phenylamine sensing by Du and coworkers [179]. The  $\text{ZnSnO}_3/\text{Zn}_2\text{SnO}_4$  sensor exhibited the response of 12.1–20 ppm phenylamine (at 260 °C) with a LOD of 50 ppb and response/recovery time of 1 s/20 s. Due to its anti-humid property, these materials can be employed in the determination of toxic phenylamine.

Investigation on  $\text{SmFeO}_3$ -modified  $\text{MoS}_2$  ( $\text{SmFeO}_3@\text{MoS}_2$ ) nanocomposites towards humidity sensing has been conducted by the Zhang research group [180]. The material, synthesized by electrospinning combined with the hydrothermal technique, operates from 11 to 95% RH with a recovery/response time of 1.5 s/29.8 s, thus it can be considered as an effective candidate. Other than the VOCs and humidity sensors, perovskite enabled composites were utilized in toxic gas quantitation. For example,  $\text{La}_{0.8}\text{Sr}_{0.2}\text{FeO}_3$  (LSFO) nanoparticles (with a size of 100–300 nm) decorated  $\text{Ga}_2\text{O}_3$  nanorod arrays have been employed in the recognition of carbon monoxide (CO) via conductivity studies [181]. The sensor operates at 500 °C with a response comparable to the Pt nanoparticles decorated  $\text{Ga}_2\text{O}_3$  nanorod arrays. However, investigations on competing gases still need to be performed with this material. Joshi et al. reported work on  $\text{BaTiO}_3$  included nanocomposites ( $\text{Ag}@\text{CuO}/\text{BaTiO}_3$ ,  $\text{CaO}/\text{BaTiO}_3$  and  $\text{CuO}/\text{BaTiO}_3$ ) towards  $\text{CO}_2$  gas sensing [182–184]. In fact, these materials used in the discovery of  $\text{CO}_2$  gas showed an optimum sensitivity of 700, 1000 and 5000 ppm, correspondingly, at either 120 °C or 160 °C with a good response and recovery time, thereby confirmed the success of  $\text{BaTiO}_3$  enabled composites for  $\text{CO}_2$  recognition.

Toxic  $\text{SO}_2$  gas detection has been established by wet chemically synthesized  $\text{SnO}_2/\text{LaFeO}_{3-x}\text{N}_x$  nanocomposite materials [185]. However, the response and other details on LODs and sensitivity were not clearly specified in this report. Recently,  $\text{La}_{0.8}\text{Sr}_{0.2}\text{CoO}_3$  (LSCO) nanoparticles decorated  $\beta\text{-Ga}_2\text{O}_3$  nanorod arrays were consumed in the determination of toxic  $\text{NO}_2$  gas at 800 °C by Zhang, et al. [186]. This is remarkable work with decent performance in sensitivity ( $0.1625 \text{ ppm}^{-1}$ ) at high temperature. Similar to the conductance-based analyte discovery, composites with perovskites were also employed in electrochemical sensors.  $\text{Sr}_2\text{PdO}_3$  nanoperovskite mixed with carbon nanotubes (CNTs) were casted over a glassy carbon (GC) electrode surface ( $\text{GC}/(\text{CNTs}-\text{Sr}_2\text{PdO}_3)$ ) and used in the electrochemical determination of dobutamine (DB, cardio-stimulator drug) [187]. This sensor showed dynamic electro-catalytic linearity in the range of 0.03–50  $\mu\text{mol L}^{-1}$  with a sensitivity of 20.91  $\mu\text{A}/\mu\text{mol L}^{-1}$ . The estimated LOD and quantification limit were 0.012  $\text{nmol L}^{-1}$  and 0.04  $\text{nmol L}^{-1}$ , respectively. It was potentiality verified in blood serum samples, which indicated good recovery. Moreover, the anti-interference sensitivity of this material confirmed its capability in electrochemical sensing of dobutamine. Nanocomposite sensors based on in-situ growth of  $\text{BaTiO}_3$  and  $\text{TiO}_2$  nanostructures over human hair-sized Ti-wire were utilized as a self-powered UV sensor [188]. Thus, one can conclude that metal oxide perovskites-based composites are an exceptional candidate in future sensory research.

Inorganic/organic metal halide perovskites were also involved in many composite-based sensory applications [189]. Chemically synthesized and ligand stabilized  $\text{CsPbBr}_3$  QDs (CPBQDs; PLQY = 88% encapsulated in polymethyl methacrylate (PMMA) nanofiber membrane (CPBQD/PMMA FM) via the electrospinning method were used in the sensing of trypsin,  $\text{Cu}^{2+}$  and pH [190]. As illustrated in Figure 19, the CPBQD/PMMA FM detects trypsin through the cleavage of peptide CF6

(Cys–Pro–Arg–Gly–R6G) followed by a Fluorescence Resonance Energy Transfer (FRET) between the fiber and cyclam–Cu<sup>2+</sup>, which leads to Cu<sup>2+</sup> recognition. Finally, 10 ppb hydrazide R6G (in ethanol) plays a vital role in pH sensors. LODs of trypsin of 0.1 μg mL<sup>-1</sup> and Cu<sup>2+</sup> quantitation of 10<sup>-15</sup> M were reported. CH<sub>3</sub>NH<sub>3</sub>PbBr<sub>3</sub> QDs were incorporated in metal-organic framework (MOF-5) microcrystals and applied in temperature and heavy metal ions detection [191]. The CH<sub>3</sub>NH<sub>3</sub>PbBr<sub>3</sub>@MOF-5 composites possess a wide range of pH adaptability and display its sensitivity to temperature from 30 to 230 °C. However, this probe showed sensor responses to many metal ions, thereby more work is required to achieved specificity.

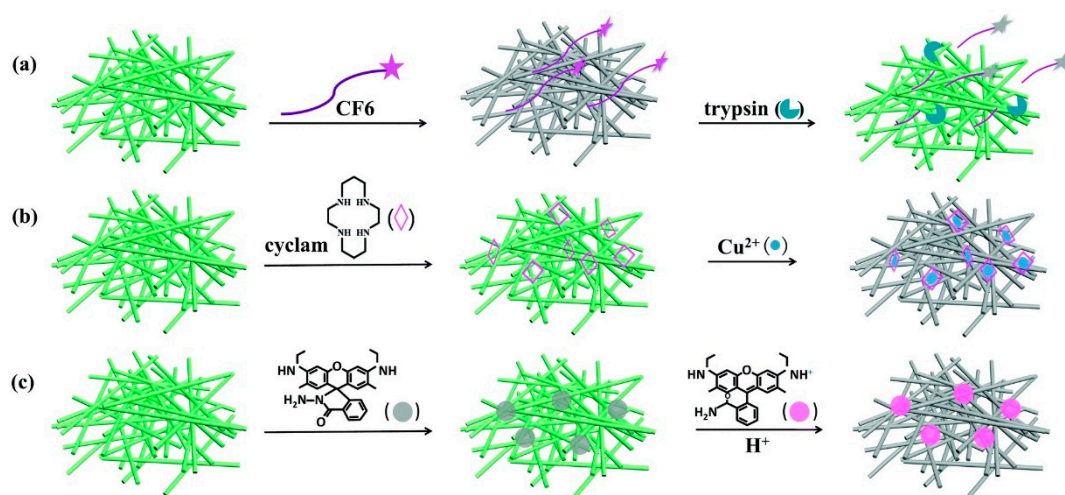


**Figure 19.** Schematic illustration of (a) trypsin, (b) Cu<sup>2+</sup> and (c) pH fluorescence detection, based on the CPBQD/PMMA FM (reproduced with the permission from reference [190]).

A porous halide perovskite–polymer nanocomposite (MAPbBr<sub>3</sub>–PVDF) has been described in fluorescent-based sensing of nitro explosives (TNT, RDX or TNG) via a trapping mechanism [192]. PL of the probe was quenched in the presence of the above analytes, but specificity of the probe was still not clarified. Toxic NO<sub>2</sub> and NH<sub>3</sub> gas detection at room temperature has been explored by the graphene nanolayers decorated CH<sub>3</sub>NH<sub>3</sub>PbBr<sub>3</sub> nanocrystals [193]. This composite material exhibited diverse mechanisms to NO<sub>2</sub> and NH<sub>3</sub> gases based on hole concentrations. Electron donating/withdrawing from NH<sub>3</sub>/NO<sub>2</sub> gases may reduce/increase the hole concentrations and leads to diverse resistance responses. Such a unique approach for multiple gas sensing is much anticipated. By combining the solution, immersion and calcination tactics, HC(NH<sub>2</sub>)<sub>2</sub>SnI<sub>3</sub>/SnO<sub>2</sub>/Pt-NPs nanocomposite was developed and employed in formaldehyde gas discrimination at 80 °C [194]. The HC(NH<sub>2</sub>)<sub>2</sub>SnI<sub>3</sub>/SnO<sub>2</sub>/Pt-NPs nanocomposite displayed the response of 47.5–10 ppm formaldehyde at 80 °C with a LOD of 65 ppb and response/recovery time of 40 s/37 s. With respect to the reported operating temperature and LOD, this study can be attested as a suitable one.

Detection of pesticides was also demonstrated by metal halide perovskite containing nanocomposites [195,196]. Lin research group utilized CsPbBr<sub>3</sub> QDs incorporated and molecularly imprinted polymers (MIPs) nanocomposites (MIPs@ CsPbBr<sub>3</sub> QDs) for the detection of pesticides omethoate (OMT) and phoxim. The 3-aminopropyltriethoxysilane (APTES)-capped CsPbBr<sub>3</sub> QDs were used in the detection of omethoate through the energy transfer mechanism in PL quenching [195]. The linear response of OMT was from 50 to 400 ng/mL with a LOD of 18.8 ng/mL. On the other hand, phoxim discrimination was attained by involvement of N-(benzyl)-N'-(3-(triethoxysilyl)propyl)urea (BUPTEOS) to enhance the PL quenching [196]. Moreover, the effect of MIPs was also comparable to those of non-imprinted polymers (NIPs) as shown in Figure 20. The linear response of phoxim was ranged between 5 and 100 ng/mL with a LOD of 1.45 ng/mL. Both reports confirmed the utility of MIPs@ CsPbBr<sub>3</sub> QDs composites in pesticide discrimination with real time applications.

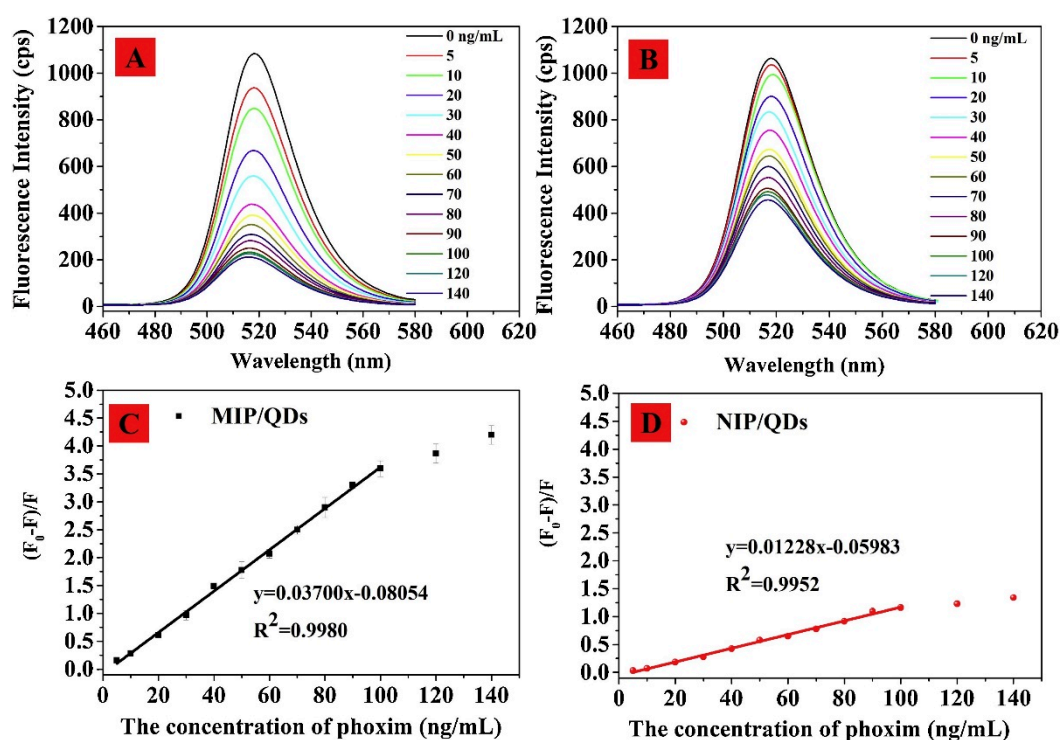


**Figure 20.** (A,B) Effect of phoxim concentration (0–140 ng/mL) on the fluorescence spectra of molecularly imprinted polymer MIP/QDs and NIP/QDs (25 °C). (C,D) Stern–Volmer plots of MIP/QDs and NIP/QDs with phoxim (reproduced with the permission from reference [196]).

In this light, CsPbBr<sub>1.5</sub>I<sub>1.5</sub>PQD immobilized TiO<sub>2</sub> inverse opal photonic crystals (IOPCs) have been engaged as electrodes for the electrochemical dopamine discovery [197]. This composite electrode expresses a linear response to dopamine from 0.1 to 250 μM with a LOD of 0.012 μM. The underlying mechanism of this sensor is discovered as “photonic stop band effect” of TiO<sub>2</sub> IOPCs on the incident light and the emission of PQDs, which enhances the photocurrent upon exposure to dopamine. This work allows the consumption of PQDs in a bioanalysis. In a similar fashion, nanostructured quasi-2D and 3D CH<sub>3</sub>NH<sub>3</sub>PbI<sub>3</sub> enabled TiO<sub>2</sub> film and molecularly imprinted polymers (MIPs) and polyethylene glycol (PEG) coated CH<sub>3</sub>NH<sub>3</sub>PbI<sub>3</sub> (MIP-PEG/CH<sub>3</sub>NH<sub>3</sub>PbI<sub>3</sub>) were consumed in the electrochemical determination of carbon tetra-bromide (CBr<sub>4</sub>) and salicylic acid, correspondingly [198,199]. The quasi-2D and 3D CH<sub>3</sub>NH<sub>3</sub>PbI<sub>3</sub>/TiO<sub>2</sub> composites can detect the CBr<sub>4</sub> down to 20 ppb mol<sup>-1</sup>, and hence become a reliable system for CBr<sub>4</sub> sensing. Subsequently, the MIP-PEG/CH<sub>3</sub>NH<sub>3</sub>PbI<sub>3</sub> nanocomposite displayed remarkable sensing performance with high sensitivity to SA in the dynamic range of 1.0 × 10<sup>-15</sup> to 7.0 × 10<sup>-11</sup> M and with LOD and the limit of quantitation (LOQ) of 2.71 × 10<sup>-16</sup> M and 9.02 × 10<sup>-16</sup> M, respectively.

Recently, an inner filter effect-based melamine assay has been demonstrated by barium sulfate-coated CsPbBr<sub>3</sub> perovskite nanocrystals (CsPbBr<sub>3</sub>NCs@BaSO<sub>4</sub>) and AuNPs [200]. As shown in Figure 21, in the presence of AuNPs the PL intensity of CsPbBr<sub>3</sub>NCs@BaSO<sub>4</sub> was quenched and then recovered upon addition of melamine. The sensor displayed the linearity from 5 to 500 nmol/L with a LOD of 0.42 nmol/L. Moreover, this work also completed the anti-interference and real sample analysis. By means of hot-injection method CsPbBr<sub>3</sub> QDs/reduced graphene oxide (RGO) nanocomposites were developed and employed as a potential candidate in photoelectric detection [201]. Due to the photoelectric effect, the PL intensity of CsPbBr<sub>3</sub> QDs was quenched in the presence of RGO. Similar hybrid halide perovskites enabled nanocomposites were also consumed in cellular imaging and temperature-insensitive optical gain studies [202,203]. In contrast, the growth of hybrid halide

perovskite itself was used as a sensor [204]. However, an in-depth theoretical interrogation on hybrid perovskites [205–207] is still required for their exceptional applications in photonics.

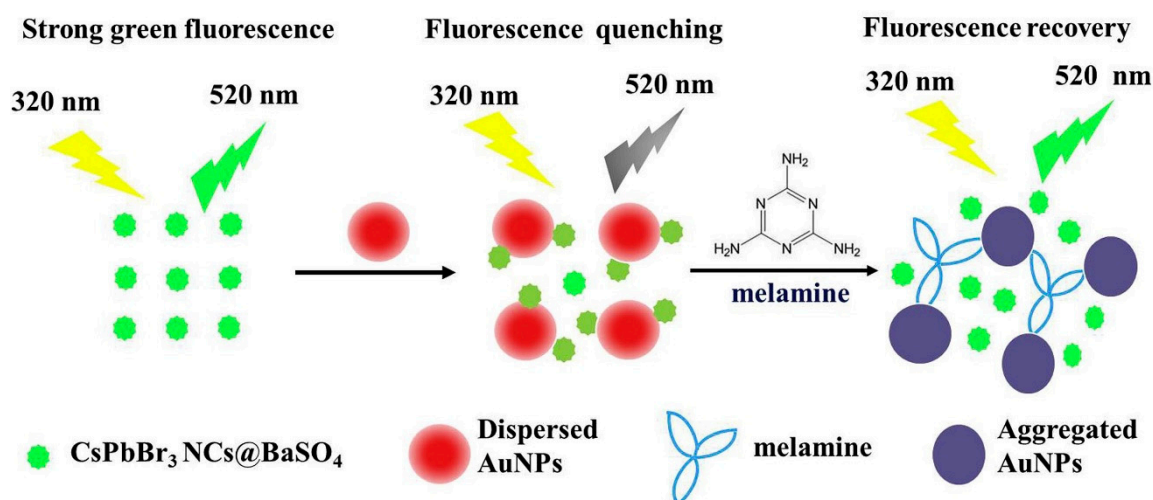


**Figure 21.** Schematic illustration of turn-on fluorescent melamine nanosensor based on the inner filter effect of the AuNPs on  $\text{CsPbBr}_3 \text{ NCs@BaSO}_4$  (reproduced with the permission from reference [200]).

## 7. Advantages and Limitations

The design and development of perovskites-based sensory probes have certain advantages and limitations as listed below.

1. The excellent opto-electronic properties of both metal oxide and metal halide/organometallic halide perovskites allow their usage in device-based analyte detection, especially towards energetic/toxic gases and humidity quantitation.
2. Metal oxide perovskites are favorable in the determination of VOCs gases with limits down to the ppt level. Therefore, they become competitive with the existing carbon-/graphene-based sensor materials [208,209].
3. Luminescent characteristics of metal halide/organometallic halide quantum dots or nanocrystals have advantages over PL-based identification of specific target. Their metallic and crystalline nature further improve their sensitivity in comparison with carbon dots [210].
4. Selectivity and sensitivity of both perovskites can be improved towards practical reliability with precision when modified or combined with nanostructured materials, such as MIPs.
5. A suitable modification of operational electrodes with perovskite materials could extend their usage in diverse analyte assays.
6. Majority of metal oxide perovskite-based devices operate at high temperatures in the assay of gases, which becomes a disadvantage in many cases. Likewise, thin film-based sensory performance is limited by film thickness, thereby careful optimization is necessary.
7. Environment and solvent conditions are the major threats to the perovskite-facilitated sensory investigations, except in the humidity analysis.
8. Cost-effectiveness in the design of perovskite-based devices is still a concern for the researchers.
9. Due to the material toxicity and instability in certain circumstances, perovskite sensors have limits in reliability and toxicity. Therefore, unlike the carbon-based materials [211], it still remains an important challenge to apply them in biological and clinical diagnosis.
10. For fluorescent-based assays, development of suitable perovskite material with high PLQY is limited by synthetic tactics, stabilizer ligands, temperature, etc.

## 8. Conclusions and Perspectives

This review summarized the sensing applications of metal oxide and metal halide/organometallic halide perovskite nanomaterials. We focused on detection of toxic/energetic gases, humidity, VOCs and electromechanical quantitation using the perovskite nanomaterials-based devices and explained the underlying mechanisms. The fluorescent-based assays of analytes were also discussed in detail with given advantages and limitations. Moreover, the sensory utilities of perovskite-enabled nanocomposites were also reviewed. Besides the aforementioned sensing applications, the following points are yet to be focused.

1. The underlying mechanisms in many sensory reports still require in-depth investigations with respect to theoretical concepts.
2. There are only limited reports on the fluorescent-based analyte assays using metal oxide perovskites, thereby need more attention.
3. The majority of the device-based sensory investigations are influenced by operational temperature, therefore, considerate optimization is needed to attain responses at room temperature.
4. A cost-effective, reproducible and standardized procedure is required to produce “state of the art” materials towards specific target (toxic gases, VOCs, anions, cations and physical parameters) for commercialization.
5. There are only limited reports on the studies of perovskite nanowire-based chemo-/biosensors, hence more efforts need to be devoted in this research area.
6. Perovskite nanomaterial-mediated sensing of biologically important species must be promoted with real applications.
7. Focus on lead free organometallic halide perovskites is desirable for research in biological imaging studies.
8. Research in the development of stable perovskite nanomaterials for environmental and biological assays needs to be intensively stimulated and encouraged.
9. Investigations on the incorporation of well-known matrixes in perovskite-composite sensors, such as metal organic frameworks, metal nanostructures, hybrid clusters and polymers, need more attention.
10. Perovskite nanomaterial-based colorimetric/naked eye analyte determinations require further attention.
11. Design and development of low toxic perovskite nanomaterial-based devices/probes towards sensing-drug delivery modules are required to be established in the future.

Though many mechanistic points require justification, perovskite-based sensory research is still a hot topic with respect to their applicability and future scope. Currently, many scientists are working on perovskite-based photonics, which may provide in-depth theories for the design and development of nanopervskite sensors and opto-electronic materials with social and economic impacts.

**Funding:** This research was funded by the Ministry of Science and Technology of Taiwan under the contract MOST 108-2811-M-009-518 and MOST 108-2112-M-009-011.

**Conflicts of Interest:** The authors declare no conflict of interest.

## References

1. Chen, A.; Chatterjee, S. Nanomaterials based electrochemical sensors for biomedical applications. *Chem. Soc. Rev.* **2013**, *42*, 5425–5438. [[CrossRef](#)] [[PubMed](#)]
2. Proposito, P.; Burratti, L.; Venditti, I. Silver Nanoparticles as Colorimetric Sensors for Water Pollutants. *Chemosensors* **2020**, *8*, 26. [[CrossRef](#)]
3. BelBruno, J.J. Nanomaterials in Sensors. *Nanomaterials* **2013**, *3*, 572–573. [[CrossRef](#)] [[PubMed](#)]
4. Shellaiah, M.; Sun, K.W. Review on Nanomaterial-Based Melamine Detection. *Chemosensors* **2019**, *7*, 9. [[CrossRef](#)]

5. Chansuvarn, W.; Tuntulani, T.; Imyim, A. Colorimetric detection of mercury (II) based on gold nanoparticles, fluorescent gold nanoclusters and other gold-based nanomaterials. *TrAC Trends Anal. Chem.* **2015**, *65*, 83–96. [[CrossRef](#)]
6. Wang, B.; Akiba, U.; Anzai, J.-I. Recent Progress in Nanomaterial-Based Electrochemical Biosensors for Cancer Biomarkers: A Review. *Molecules* **2017**, *22*, 1048. [[CrossRef](#)]
7. Shellaiah, M.; Sun, K.W. Luminescent Metal Nanoclusters for Potential Chemosensor Applications. *Chemosensors* **2017**, *5*, 36. [[CrossRef](#)]
8. Zeng, S.; Baillargeat, D.; Ho, H.-P.; Yong, K.-T. Nanomaterials enhanced surface plasmon resonance for biological and chemical sensing applications. *Chem. Soc. Rev.* **2014**, *43*, 3426–3452. [[CrossRef](#)]
9. Zhang, W.; Eperon, G.E.; Snaith, H.J. Metal halide perovskites for energy applications. *Nat. Energy* **2016**, *1*, 16048. [[CrossRef](#)]
10. Gao, P.; Grätzel, M.; Nazeeruddin, M.K. Organohalide lead perovskites for photovoltaic applications. *Energy Environ. Sci.* **2014**, *7*, 2448–2463. [[CrossRef](#)]
11. Choi, J.J.; Billinge, S.J.L. Perovskites at the nanoscale: From fundamentals to applications. *Nanoscale* **2016**, *8*, 6206–6208. [[CrossRef](#)] [[PubMed](#)]
12. Labhassetwar, N.; Saravanan, G.; Kumar Megarajan, S.; Manwar, N.; Khobragade, R.; Doggali, P.; Grasset, F. Perovskite-type catalytic materials for environmental applications. *Sci. Technol. Adv. Mater.* **2015**, *16*, 036002. [[CrossRef](#)] [[PubMed](#)]
13. Zhao, Y.; Zhu, K. Organic–inorganic hybrid lead halide perovskites for optoelectronic and electronic applications. *Chem. Soc. Rev.* **2016**, *45*, 655–689. [[CrossRef](#)] [[PubMed](#)]
14. Adjokatse, S.; Fang, H.-H.; Loi, M.A. Broadly tunable metal halide perovskites for solid-state light-emission applications. *Mater. Today* **2017**, *20*, 413–424. [[CrossRef](#)]
15. Bhandari, K.P.; Ellingson, R.J. 11—An Overview of Hybrid Organic–Inorganic Metal Halide Perovskite Solar Cells. In *A Comprehensive Guide to Solar Energy Systems*; Letcher, T.M., Fthenakis, V.M., Eds.; Academic Press: Cambridge, MA, USA, 2018; pp. 233–254.
16. Assirey, E.A.R. Perovskite synthesis, properties and their related biochemical and industrial application. *Saudi Pharmaceut. J.* **2019**, *27*, 817–829. [[CrossRef](#)] [[PubMed](#)]
17. Chen, Y.; Zhang, L.; Zhang, Y.; Gao, H.; Yan, H. Large-area perovskite solar cells—A review of recent progress and issues. *RSC Adv.* **2018**, *8*, 10489–10508. [[CrossRef](#)]
18. Hong, K.; Le, Q.V.; Kim, S.Y.; Jang, H.W. Low-dimensional halide perovskites: Review and issues. *J. Mater. Chem. C* **2018**, *6*, 2189–2209. [[CrossRef](#)]
19. Rørvik, P.M.; Grande, T.; Einarsrud, M.-A. One-Dimensional Nanostructures of Ferroelectric Perovskites. *Adv. Mater.* **2011**, *23*, 4007–4034. [[CrossRef](#)]
20. Liu, J.; Chen, K.; Khan, S.A.; Shabbir, B.; Zhang, Y.; Khan, Q.; Bao, Q. Synthesis and optical applications of low dimensional metal-halide perovskites. *Nanotechnology* **2020**, *31*, 152002. [[CrossRef](#)]
21. Fergus, J.W. Perovskite oxides for semiconductor-based gas sensors. *Sens. Actuators B* **2007**, *123*, 1169–1179. [[CrossRef](#)]
22. Yan, J.; He, Y.; Chen, Y.; Zhang, Y.; Yan, H. CH<sub>3</sub>NH<sub>3</sub>Br solution as a novel platform for the selective fluorescence detection of Pb<sup>2+</sup> ions. *Sci. Rep.* **2019**, *9*, 15840. [[CrossRef](#)]
23. Varignon, J.; Bibes, M.; Zunger, A. Origin of band gaps in 3d perovskite oxides. *Nat. Commun.* **2019**, *10*, 1658. [[CrossRef](#)]
24. Zhang, J.; Qin, Z.; Zeng, D.; Xie, C. Metal-oxide-semiconductor based gas sensors: Screening, preparation, and integration. *Phys. Chem. Chem. Phys.* **2017**, *19*, 6313–6329. [[CrossRef](#)] [[PubMed](#)]
25. Wang, X.; Qin, H.; Sun, L.; Hu, J. CO<sub>2</sub> sensing properties and mechanism of nanocrystalline LaFeO<sub>3</sub> sensor. *Sens. Actuators B* **2013**, *188*, 965–971. [[CrossRef](#)]
26. Zhu, Z.; Sun, Q.; Zhang, Z.; Dai, J.; Xing, G.; Li, S.; Huang, X.; Huang, W. Metal halide perovskites: Stability and sensing-ability. *J. Mater. Chem. C* **2018**, *6*, 10121–10137. [[CrossRef](#)]
27. Shamsi, J.; Urban, A.S.; Imran, M.; De Trizio, L.; Manna, L. Metal Halide Perovskite Nanocrystals: Synthesis, Post-Synthesis Modifications, and Their Optical Properties. *Chem. Rev.* **2019**, *119*, 3296–3348. [[CrossRef](#)]
28. Boyd, C.C.; Checharoen, R.; Leijtens, T.; McGehee, M.D. Understanding Degradation Mechanisms and Improving Stability of Perovskite Photovoltaics. *Chem. Rev.* **2019**, *119*, 3418–3451. [[CrossRef](#)]

29. Chen, Q.; De Marco, N.; Yang, Y.; Song, T.-B.; Chen, C.-C.; Zhao, H.; Hong, Z.; Zhou, H.; Yang, Y. Under the spotlight: The organic–inorganic hybrid halide perovskite for optoelectronic applications. *Nano Today* **2015**, *10*, 355–396. [[CrossRef](#)]
30. Moradi, Z.; Fallah, H.; Hajimahmoodzadeh, M. Nanocomposite perovskite based optical sensor with broadband absorption spectrum. *Sens. Actuators A* **2018**, *280*, 47–51. [[CrossRef](#)]
31. Cho, M.-Y.; Kim, S.; Kim, I.-S.; Kim, E.-S.; Wang, Z.-J.; Kim, N.-Y.; Kim, S.-W.; Oh, J.-M. Perovskite-Induced Ultrasensitive and Highly Stable Humidity Sensor Systems Prepared by Aerosol Deposition at Room Temperature. *Adv. Funct. Mater.* **2020**, *30*, 1907449. [[CrossRef](#)]
32. Yang, H.; Fan, W.; Hills-Kimball, K.; Chen, O.; Wang, L.-Q. Introducing Manganese-Doped Lead Halide Perovskite Quantum Dots: A Simple Synthesis Illustrating Optoelectronic Properties of Semiconductors. *J. Chem. Educ.* **2019**, *96*, 2300–2307. [[CrossRef](#)]
33. Lin, F.; Li, F.; Lai, Z.; Cai, Z.; Wang, Y.; Wolfbeis, O.S.; Chen, X. MnII-Doped Cesium Lead Chloride Perovskite Nanocrystals: Demonstration of Oxygen Sensing Capability Based on Luminescent Dopants and Host-Dopant Energy Transfer. *ACS Appl. Mater. Interfaces* **2018**, *10*, 23335–23343. [[CrossRef](#)] [[PubMed](#)]
34. Athayde, D.D.; Souza, D.F.; Silva, A.M.A.; Vasconcelos, D.; Nunes, E.H.M.; Diniz da Costa, J.C.; Vasconcelos, W.L. Review of perovskite ceramic synthesis and membrane preparation methods. *Ceram. Int.* **2016**, *42*, 6555–6571. [[CrossRef](#)]
35. Ananthakumar, S.; Kumar, J.R.; Babu, S.M. Cesium lead halide (CsPbX<sub>3</sub>, X=Cl, Br, I) perovskite quantum dots-synthesis, properties, and applications: A review of their present status. *J. Photonics Energy* **2016**, *6*, 042001. [[CrossRef](#)]
36. Protesescu, L.; Yakunin, S.; Nazarenko, O.; Dirin, D.N.; Kovalenko, M.V. Low-Cost Synthesis of Highly Luminescent Colloidal Lead Halide Perovskite Nanocrystals by Wet Ball Milling. *ACS Appl. Nano Mater.* **2018**, *1*, 1300–1308. [[CrossRef](#)]
37. Chandra Dhal, G.; Dey, S.; Mohan, D.; Prasad, R. Solution Combustion Synthesis of Perovskite-type Catalysts for Diesel Engine Exhaust Gas Purification. *Mater. Today Proc.* **2017**, *4*, 10489–10493. [[CrossRef](#)]
38. Ecija, A.; Vidal, K.; Larrañaga, A.; Luis Ortega-San-Martín, L.; Arriortua, M.I. Synthetic Methods for Perovskite Materials—Structure and Morphology. In *Advances in Crystallization Processes*; Mastai, Y., Ed.; IntechOpen: Rijeka, Croatia, 2012; pp. 485–506.
39. Cernea, M.; Vasiliu, F.; Plapcianu, C.; Bartha, C.; Mercioniu, I.; Pasuk, I.; Lowndes, R.; Trusca, R.; Aldica, G.V.; Pintilie, L. Preparation by sol–gel and solid state reaction methods and properties investigation of double perovskite Sr<sub>2</sub>FeMoO<sub>6</sub>. *J. Eur. Ceram. Soc.* **2013**, *33*, 2483–2490. [[CrossRef](#)]
40. da Silva Filho, J.M.C.; Ermakov, V.A.; Marques, F.C. Perovskite Thin Film Synthesised from Sputtered Lead Sulphide. *Sci. Rep.* **2018**, *8*, 1563. [[CrossRef](#)]
41. Peña, M.A.; Fierro, J.L.G. Chemical Structures and Performance of Perovskite Oxides. *Chem. Rev.* **2001**, *101*, 1981–2018. [[CrossRef](#)]
42. Trots, D.M.; Myagkota, S.V. High-temperature structural evolution of caesium and rubidium triiodoplumbates. *J. Phys. Chem. Solids* **2008**, *69*, 2520–2526. [[CrossRef](#)]
43. Plesko, S.; Kind, R.; Roos, J. Structural Phase Transitions in CsPbCl<sub>3</sub> and RbCdCl<sub>3</sub>. *J. Phys. Soc. Jpn.* **1978**, *45*, 553–557. [[CrossRef](#)]
44. Rodová, M.; Brožek, J.; Knížek, K.; Nitsch, K. Phase transitions in ternary caesium lead bromide. *J. Therm. Anal. Calorim.* **2003**, *71*, 667–673. [[CrossRef](#)]
45. Chen, C.; Hu, X.; Lu, W.; Chang, S.; Shi, L.; Li, L.; Zhong, H.; Han, J.-B. Elucidating the phase transitions and temperature-dependent photoluminescence of MAPbBr<sub>3</sub> single crystal. *J. Phys. D Appl. Phys.* **2018**, *51*, 045105. [[CrossRef](#)]
46. Stoumpos, C.C.; Malliakas, C.D.; Kanatzidis, M.G. Semiconducting Tin and Lead Iodide Perovskites with Organic Cations: Phase Transitions, High Mobilities, and Near-Infrared Photoluminescent Properties. *Inorg. Chem.* **2013**, *52*, 9019–9038. [[CrossRef](#)] [[PubMed](#)]
47. Baikie, T.; Fang, Y.; Kadro, J.M.; Schreyer, M.; Wei, F.; Mhaisalkar, S.G.; Graetzel, M.; White, T.J. Synthesis and crystal chemistry of the hybrid perovskite (CH<sub>3</sub>NH<sub>3</sub>)PbI<sub>3</sub> for solid-state sensitised solar cell applications. *J. Mater. Chem. A* **2013**, *1*, 5628–5641. [[CrossRef](#)]
48. Hsu, H.-P.; Li, L.-C.; Shellaiah, M.; Sun, K.W. Structural, Photophysical, and Electronic Properties of CH<sub>3</sub>NH<sub>3</sub>PbCl<sub>3</sub> Single Crystals. *Sci. Rep.* **2019**, *9*, 13311. [[CrossRef](#)] [[PubMed](#)]

49. Wang, K.-H.; Li, L.-C.; Shellaiah, M.; Wen Sun, K. Structural and Photophysical Properties of Methylammonium Lead Tribromide (MAPbBr<sub>3</sub>) Single Crystals. *Sci. Rep.* **2017**, *7*, 13643. [[CrossRef](#)]
50. Stoerzinger, K.A.; Hong, W.T.; Azimi, G.; Giordano, L.; Lee, Y.-L.; Crumlin, E.J.; Biegalski, M.D.; Bluhm, H.; Varanasi, K.K.; Shao-Horn, Y. Reactivity of Perovskites with Water: Role of Hydroxylation in Wetting and Implications for Oxygen Electrocatalysis. *J. Phys. Chem. C* **2015**, *119*, 18504–18512. [[CrossRef](#)]
51. Frost, J.M.; Butler, K.T.; Brivio, F.; Hendon, C.H.; van Schilfgaarde, M.; Walsh, A. Atomistic Origins of High-Performance in Hybrid Halide Perovskite Solar Cells. *Nano Lett.* **2014**, *14*, 2584–2590. [[CrossRef](#)]
52. Bass, K.K.; McAnally, R.E.; Zhou, S.; Djurovich, P.I.; Thompson, M.E.; Melot, B.C. Influence of moisture on the preparation, crystal structure, and photophysical properties of organohalide perovskites. *Chem. Commun.* **2014**, *50*, 15819–15822. [[CrossRef](#)]
53. Ralaarisoa, M.; Rodríguez, Y.; Salzmänn, I.; Vaillant, L.; Koch, N. Impact of solvent exposure on the structure and electronic properties of CH<sub>3</sub>NH<sub>3</sub>PbI<sub>3-x</sub>Cl<sub>x</sub> mixed halide perovskite films. *Appl. Phys. A* **2019**, *125*, 470. [[CrossRef](#)]
54. Ihlefeld, J.F.; Borland, W.J.; Maria, J.-P. Enhanced Dielectric and Crystalline Properties in Ferroelectric Barium Titanate Thin Films. *Adv. Funct. Mater.* **2007**, *17*, 1199–1203. [[CrossRef](#)]
55. Ji, Q.; Bi, L.; Zhang, J.; Cao, H.; Zhao, X.S. The role of oxygen vacancies of ABO<sub>3</sub> perovskite oxides in the oxygen reduction reaction. *Energy Environ. Sci.* **2020**, *13*, 1408–1428. [[CrossRef](#)]
56. Karppinen, M.; Matvejeff, M.; Salomäki, K.; Yamauchi, H. Oxygen content analysis of functional perovskite-derived cobalt oxides. *J. Mater. Chem.* **2002**, *12*, 1761–1764. [[CrossRef](#)]
57. Uchino, K. Glory of piezoelectric perovskites. *Sci. Technol. Adv. Mater.* **2015**, *16*, 046001. [[CrossRef](#)] [[PubMed](#)]
58. Spaldin, N.A.; Cheong, S.-W.; Ramesh, R. Multiferroics: Past, present, and future. *Phys. Today* **2010**, *63*, 38–43. [[CrossRef](#)]
59. Arandiyani, H.; Wang, Y.; Sun, H.; Rezaei, M.; Dai, H. Ordered meso- and macroporous perovskite oxide catalysts for emerging applications. *Chem. Commun.* **2018**, *54*, 6484–6502. [[CrossRef](#)]
60. Chouhan, L.; Ghimire, S.; Subrahmanyam, C.; Miyasaka, T.; Biju, V. Synthesis, optoelectronic properties and applications of halide perovskites. *Chem. Soc. Rev.* **2020**, *49*, 2869–2885. [[CrossRef](#)]
61. Manser, J.S.; Christians, J.A.; Kamat, P.V. Intriguing Optoelectronic Properties of Metal Halide Perovskites. *Chem. Rev.* **2016**, *116*, 12956–13008. [[CrossRef](#)]
62. Aldakov, D.; Reiss, P. Safer-by-Design Fluorescent Nanocrystals: Metal Halide Perovskites vs. Semiconductor Quantum Dots. *J. Phys. Chem. C* **2019**, *123*, 12527–12541. [[CrossRef](#)]
63. Shahrokhi, S.; Gao, W.; Wang, Y.; Anandan, P.R.; Rahaman, M.Z.; Singh, S.; Wang, D.; Cazorla, C.; Yuan, G.; Liu, J.-M.; et al. Emergence of Ferroelectricity in Halide Perovskites. In *Small Methods*; Wiley: Hoboken, NJ, USA, 2020; p. 2000149. [[CrossRef](#)]
64. Bi, F.; Markov, S.; Wang, R.; Kwok, Y.; Zhou, W.; Liu, L.; Zheng, X.; Chen, G.; Yam, C. Enhanced Photovoltaic Properties Induced by Ferroelectric Domain Structures in Organometallic Halide Perovskites. *J. Phys. Chem. C* **2017**, *121*, 11151–11158. [[CrossRef](#)]
65. Fan, Z.; Sun, K.; Wang, J. Perovskites for photovoltaics: A combined review of organic–inorganic halide perovskites and ferroelectric oxide perovskites. *J. Mater. Chem. A* **2015**, *3*, 18809–18828. [[CrossRef](#)]
66. Yang, B.; Han, K. Charge-Carrier Dynamics of Lead-Free Halide Perovskite Nanocrystals. *Acc. Chem. Res.* **2019**, *52*, 3188–3198. [[CrossRef](#)] [[PubMed](#)]
67. Unni, K.; Manjot, K.; Manjeet, K.; Akshay, K. Factors affecting the stability of perovskite solar cells: A comprehensive review. *J. Photonics Energy* **2019**, *9*, 1–42.
68. Ghosh, D.; Aziz, A.; Dawson, J.A.; Walker, A.B.; Islam, M.S. Putting the Squeeze on Lead Iodide Perovskites: Pressure-Induced Effects To Tune Their Structural and Optoelectronic Behavior. *Chem. Mater.* **2019**, *31*, 4063–4071. [[CrossRef](#)]
69. Shimada, K.; Takashima, H.; Wang, R.; Prijamboedi, B.; Miura, N.; Itoh, M. Capacitance Temperature Sensor Using Ferroelectric (Sr<sub>0.95</sub>Ca<sub>0.05</sub>)TiO<sub>3</sub> Perovskite. *Ferroelectrics* **2006**, *331*, 141–145. [[CrossRef](#)]
70. Chu, K.; Zhou, Y.-H.; Song, J.-L.; Zhang, C. An ABX<sub>3</sub> organic–inorganic perovskite-type material with the formula (C<sub>5</sub>N<sub>2</sub>H<sub>9</sub>)CdCl<sub>3</sub>: Application for detection of volatile organic solvent molecules. *Polyhedron* **2017**, *131*, 22–26. [[CrossRef](#)]

71. Jancik Prochazkova, A.; Demchyshyn, S.; Yumusak, C.; Másilko, J.; Brüggemann, O.; Weiter, M.; Kaltenbrunner, M.; Sariciftci, N.S.; Krajcovic, J.; Salinas, Y.; et al. Proteinogenic Amino Acid Assisted Preparation of Highly Luminescent Hybrid Perovskite Nanoparticles. *ACS Appl. Nano Mater.* **2019**, *2*, 4267–4274. [[CrossRef](#)]
72. McKenna, B.; Shivkumar, A.; Charles, B.; Evans, R.C. Synthetic factors affecting the stability of methylammonium lead halide perovskite nanocrystals. *Nanoscale* **2020**, *12*, 11694–11702. [[CrossRef](#)]
73. Zhu, Y.; Li, F.; Huang, Y.; Lin, F.; Chen, X. Wavelength-Shift-Based Colorimetric Sensing for Peroxide Number of Edible Oil Using CsPbBr<sub>3</sub> Perovskite Nanocrystals. *Anal. Chem.* **2019**, *91*, 14183–14187. [[CrossRef](#)]
74. Hahn, Y.-B.; Ahmad, R.; Tripathy, N. Chemical and biological sensors based on metal oxide nanostructures. *Chem. Commun.* **2012**, *48*, 10369–10385. [[CrossRef](#)] [[PubMed](#)]
75. Mahesh Kumar, M.; Post, M.L. Effect of grain boundaries on hydrocarbon sensing in Fe-doped p-type semiconducting perovskite SrTiO<sub>3</sub> films. *J. Appl. Phys.* **2005**, *97*, 114916. [[CrossRef](#)]
76. Qin, J.; Cui, Z.; Yang, X.; Zhu, S.; Li, Z.; Liang, Y. Synthesis of three-dimensionally ordered macroporous LaFeO<sub>3</sub> with enhanced methanol gas sensing properties. *Sens. Actuators B* **2015**, *209*, 706–713. [[CrossRef](#)]
77. Siemons, M.; Leifert, A.; Simon, U. Preparation and Gas Sensing Characteristics of Nanoparticulate p-Type Semiconducting LnFeO<sub>3</sub> and LnCrO<sub>3</sub> Materials. *Adv. Funct. Mater.* **2007**, *17*, 2189–2197. [[CrossRef](#)]
78. Thirumalairajan, S.; Girija, K.; Mastelaro, V.R.; Ponpandian, N. Surface Morphology-Dependent Room-Temperature LaFeO<sub>3</sub> Nanostructure Thin Films as Selective NO<sub>2</sub> Gas Sensor Prepared by Radio Frequency Magnetron Sputtering. *ACS Appl. Mater. Interfaces* **2014**, *6*, 13917–13927. [[CrossRef](#)]
79. Wang, Y.-Z.; Zhong, H.; Li, X.-M.; Jia, F.-F.; Shi, Y.-X.; Zhang, W.-G.; Cheng, Z.-P.; Zhang, L.-L.; Wang, J.-K. Perovskite LaTiO<sub>3</sub>-Ag<sub>0.2</sub> nanomaterials for nonenzymatic glucose sensor with high performance. *Biosens. Bioelectron.* **2013**, *48*, 56–60. [[CrossRef](#)] [[PubMed](#)]
80. Giang, H.T.; Duy, H.T.; Ngan, P.Q.; Thai, G.H.; Thu, D.T.A.; Thu, D.T.; Toan, N.N. Hydrocarbon gas sensing of nano-crystalline perovskite oxides LnFeO<sub>3</sub> (Ln=La, Nd and Sm). *Sens. Actuators B* **2011**, *158*, 246–251. [[CrossRef](#)]
81. Itagaki, Y.; Fujihashi, K.; Aono, H.; Mori, M.; Sadaoka, Y. VOC sensing behavior of semiconducting Sm<sub>2</sub>O<sub>3</sub>/SmFeO<sub>3</sub> mixtures. *J. Ceram. Soc. Jpn.* **2015**, *123*, 961–966. [[CrossRef](#)]
82. Tasaki, T.; Takase, S.; Shimizu, Y. Impedancemetric acetylene gas sensing properties of Sm-Fe-based perovskite-type oxide-based thick-film device. *Sens. Actuators B* **2013**, *187*, 128–134. [[CrossRef](#)]
83. Mori, M.; Itagaki, Y.; Sadaoka, Y. Effect of VOC on ozone detection using semiconducting sensor with SmFe<sub>1-x</sub>Co<sub>x</sub>O<sub>3</sub> perovskite-type oxides. *Sens. Actuators B* **2012**, *163*, 44–50. [[CrossRef](#)]
84. Giang, H.T.; Duy, H.T.; Ngan, P.Q.; Thai, G.H.; Thu, D.T.A.; Thu, D.T.; Toan, N.N. High sensitivity and selectivity of mixed potential sensor based on Pt/YSZ/SmFeO<sub>3</sub> to NO<sub>2</sub> gas. *Sens. Actuators B* **2013**, *183*, 550–555. [[CrossRef](#)]
85. Doroftei, C.; Popa, P.D.; Iacomi, F.; Leontie, L. The influence of Zn<sup>2+</sup> ions on the microstructure, electrical and gas sensing properties of La<sub>0.8</sub>Pb<sub>0.2</sub>FeO<sub>3</sub> perovskite. *Sens. Actuators B* **2014**, *191*, 239–245. [[CrossRef](#)]
86. Huang, X.; Zhao, G.; Wang, G.; Irvine, J.T.S. Synthesis and applications of nanoporous perovskite metal oxides. *Chem. Sci.* **2018**, *9*, 3623–3637. [[CrossRef](#)]
87. Bulemo, P.M.; Kim, I.-D. Recent advances in ABO<sub>3</sub> perovskites: Their gas-sensing performance as resistive-type gas sensors. *J. Korean Ceram. Soc.* **2020**, *57*, 24–39. [[CrossRef](#)]
88. Enhessari, M.; Salehabadi, A. Perovskites-Based Nanomaterials for Chemical Sensors. In *Progresses in Chemical Sensor*; Wang, W., Ed.; IntechOpen: Rijeka, Croatia, 2016; pp. 59–91.
89. Degler, D. Trends and Advances in the Characterization of Gas Sensing Materials Based on Semiconducting Oxides. *Sensors* **2018**, *18*, 3544. [[CrossRef](#)] [[PubMed](#)]
90. Zhang, B.; Gao, P.-X. Metal Oxide Nanoarrays for Chemical Sensing: A Review of Fabrication Methods, Sensing Modes, and Their Inter-correlations. *Front. Mater.* **2019**, *6*, 55. [[CrossRef](#)]
91. Cao, E.; Wang, H.; Wang, X.; Yang, Y.; Hao, W.; Sun, L.; Zhang, Y. Enhanced ethanol sensing performance for chlorine doped nanocrystalline LaFeO<sub>3-δ</sub> powders by citric sol-gel method. *Sens. Actuators B* **2017**, *251*, 885–893. [[CrossRef](#)]
92. Zhang, H.; Yi, J. Enhanced ethanol gas sensing performance of ZnO nanoflowers decorated with LaMnO<sub>3</sub> perovskite nanoparticles. *Mater. Lett.* **2018**, *216*, 196–198. [[CrossRef](#)]
93. Lin, T.; Lv, X.; Hu, Z.; Xu, A.; Feng, C. Semiconductor Metal Oxides as Chemoresistive Sensors for Detecting Volatile Organic Compounds. *Sensors* **2019**, *19*, 233. [[CrossRef](#)]

94. Ma, X.-H.; Li, H.-Y.; Kweon, S.-H.; Jeong, S.-Y.; Lee, J.-H.; Nahm, S. Highly Sensitive and Selective PbTiO<sub>3</sub> Gas Sensors with Negligible Humidity Interference in Ambient Atmosphere. *ACS Appl. Mater. Interfaces* **2019**, *11*, 5240–5246. [[CrossRef](#)]
95. Cao, E.; Wu, A.; Wang, H.; Zhang, Y.; Hao, W.; Sun, L. Enhanced Ethanol Sensing Performance of Au and Cl Comodified LaFeO<sub>3</sub> Nanoparticles. *ACS Appl. Nano Mater.* **2019**, *2*, 1541–1551. [[CrossRef](#)]
96. Ma, L.; Ma, S.Y.; Shen, X.F.; Wang, T.T.; Jiang, X.H.; Chen, Q.; Qiang, Z.; Yang, H.M.; Chen, H. PrFeO<sub>3</sub> hollow nanofibers as a highly efficient gas sensor for acetone detection. *Sens. Actuators B* **2018**, *255*, 2546–2554. [[CrossRef](#)]
97. Yin, Y.; Li, F.; Zhang, N.; Ruan, S.; Zhang, H.; Chen, Y. Improved gas sensing properties of silver-functionalized ZnSnO<sub>3</sub> hollow nanocubes. *Inorg. Chem. Front.* **2018**, *5*, 2123–2131. [[CrossRef](#)]
98. Zhang, H.; Qin, H.; Zhang, P.; Hu, J. High Sensing Properties of 3 wt % Pd-Doped SmFe<sub>1-x</sub>MgxO<sub>3</sub> Nanocrystalline Powders to Acetone Vapor with Ultralow Concentrations under Light Illumination. *ACS Appl. Mater. Interfaces* **2018**, *10*, 15558–15564. [[CrossRef](#)] [[PubMed](#)]
99. Liu, H.; Li, C.; Zhang, X.; Zheng, K.; Xie, R.; Huang, H.; Peng, T.; Jia, R.; Huo, J. A novel and highly responsive acetone sensor based on La<sub>1-x</sub>Y<sub>x</sub>MnO<sub>3+δ</sub> nanoparticles. *Mater. Lett.* **2019**, *257*, 126725. [[CrossRef](#)]
100. Chen, Q.; Wang, Y.; Wang, M.; Ma, S.; Wang, P.; Zhang, G.; Chen, W.; Jiao, H.; Liu, L.; Xu, X. Enhanced acetone sensor based on Au functionalized In-doped ZnSnO<sub>3</sub> nanofibers synthesized by electrospinning method. *J. Colloid Interface Sci.* **2019**, *543*, 285–299. [[CrossRef](#)]
101. Chen, M.; Zhang, Y.; Zhang, J.; Li, K.; Lv, T.; Shen, K.; Zhu, Z.; Liu, Q. Facile lotus-leaf-templated synthesis and enhanced xylene gas sensing properties of Ag-LaFeO<sub>3</sub> nanoparticles. *J. Mater. Chem. C* **2018**, *6*, 6138–6145. [[CrossRef](#)]
102. Han, T.; Ma, S.Y.; Xu, X.L.; Xu, X.H.; Pei, S.T.; Tie, Y.; Cao, P.F.; Liu, W.W.; Wang, B.J.; Zhang, R.; et al. Rough SmFeO<sub>3</sub> nanofibers as an optimization ethylene glycol gas sensor prepared by electrospinning. *Mater. Lett.* **2020**, *268*, 127575. [[CrossRef](#)]
103. Yin, Y.; Shen, Y.; Zhou, P.; Lu, R.; Li, A.; Zhao, S.; Liu, W.; Wei, D.; Wei, K. Fabrication, characterization and n-propanol sensing properties of perovskite-type ZnSnO<sub>3</sub> nanospheres based gas sensor. *Appl. Surf. Sci.* **2020**, *509*, 145335. [[CrossRef](#)]
104. Wei, W.; Guo, S.; Chen, C.; Sun, L.; Chen, Y.; Guo, W.; Ruan, S. High sensitive and fast formaldehyde gas sensor based on Ag-doped LaFeO<sub>3</sub> nanofibers. *J. Alloys Compd.* **2017**, *695*, 1122–1127. [[CrossRef](#)]
105. Yang, K.; Ma, J.; Qiao, X.; Cui, Y.; Jia, L.; Wang, H. Hierarchical porous LaFeO<sub>3</sub> nanostructure for efficient trace detection of formaldehyde. *Sens. Actuators B* **2020**, *313*, 128022. [[CrossRef](#)]
106. Bala, A.; Majumder, S.B.; Dewan, M.; Roy Chaudhuri, A. Hydrogen sensing characteristics of perovskite based calcium doped BiFeO<sub>3</sub> thin films. *Int. J. Hydrog. Energy* **2019**, *44*, 18648–18656. [[CrossRef](#)]
107. Gildo-Ortiz, L.; Reyes-Gómez, J.; Flores-Álvarez, J.M.; Guillén-Bonilla, H.; Olvera, M.d.l.L.; Rodríguez Betancourt, V.M.; Verde-Gómez, Y.; Guillén-Cervantes, A.; Santoyo-Salazar, J. Synthesis, characterization and sensitivity tests of perovskite-type LaFeO<sub>3</sub> nanoparticles in CO and propane atmospheres. *Ceram. Int.* **2016**, *42*, 18821–18827. [[CrossRef](#)]
108. Ding, J.-C.; Li, H.-Y.; Cao, T.-C.; Cai, Z.-X.; Wang, X.-X.; Guo, X. Characteristics and sensing properties of CO gas sensors based on LaCo<sub>1-x</sub>FexO<sub>3</sub> nanoparticles. *Solid State Ion.* **2017**, *303*, 97–102. [[CrossRef](#)]
109. Michel, C.R.; Martínez-Preciado, A.H.; López-Mena, E.R.; Elías-Zuñiga, A.; Cayetano-Castro, N.; Ceballos-Sanchez, O. Improvement of the gas sensing response of nanostructured LaCoO<sub>3</sub> by the addition of Ag nanoparticles. *Sens. Actuators B* **2017**, *246*, 181–189. [[CrossRef](#)]
110. Gildo-Ortiz, L.; Guillén-Bonilla, H.; Rodríguez-Betancourt, V.M.; Blanco-Alonso, O.; Guillén-Bonilla, A.; Santoyo-Salazar, J.; Romero-Ibarra, I.C.; Reyes-Gómez, J. Key processing of porous and fibrous LaCoO<sub>3</sub> nanostructures for successful CO and propane sensing. *Ceram. Int.* **2018**, *44*, 15402–15410. [[CrossRef](#)]
111. Gildo-Ortiz, L.; Rodríguez-Betancourt, V.M.; Blanco-Alonso, O.; Guillén-Bonilla, A.; Guillén-Bonilla, J.T.; Guillén-Cervantes, A.; Santoyo-Salazar, J.; Guillén-Bonilla, H. A simple route for the preparation of nanostructured GdCoO<sub>3</sub> via the solution method, as well as its characterization and its response to certain gases. *Results Phys.* **2019**, *12*, 475–483. [[CrossRef](#)]
112. Karki, S.B.; Hona, R.K.; Ramezanipour, F. Effect of Structure on Sensor Properties of Oxygen-Deficient Perovskites, A<sub>2</sub>BB'O<sub>5</sub> (A = Ca, Sr; B = Fe; B' = Fe, Mn) for Oxygen, Carbon Dioxide and Carbon Monoxide Sensing. *J. Electron. Mater.* **2020**, *49*, 1557–1567. [[CrossRef](#)]

113. Dai, L.; Ma, L.; Meng, W.; Li, Y.; He, Z.; Wang, L. Impedancemetric NO<sub>2</sub> sensor based on Pd doped perovskite oxide sensing electrode conjunction with phase angle response. *Electrochim. Acta* **2018**, *265*, 411–418. [[CrossRef](#)]
114. Palimar, S.; Kaushik, S.D.; Siruguri, V.; Swain, D.; Viegas, A.E.; Narayana, C.; Sundaram, N.G. Investigation of Ca substitution on the gas sensing potential of LaFeO<sub>3</sub> nanoparticles towards low concentration SO<sub>2</sub> gas. *Dalton Trans.* **2016**, *45*, 13547–13555. [[CrossRef](#)]
115. Ma, C.; Hao, X.; Yang, X.; Liang, X.; Liu, F.; Liu, T.; Yang, C.; Zhu, H.; Lu, G. Sub-ppb SO<sub>2</sub> gas sensor based on NASICON and La<sub>x</sub>Sm<sub>1-x</sub>FeO<sub>3</sub> sensing electrode. *Sens. Actuators B* **2018**, *256*, 648–655. [[CrossRef](#)]
116. Queraltó, A.; Graf, D.; Frohnhoven, R.; Fischer, T.; Vanrompay, H.; Bals, S.; Bartasyte, A.; Mathur, S. LaFeO<sub>3</sub> Nanofibers for High Detection of Sulfur-Containing Gases. *ACS Sustain. Chem. Eng.* **2019**, *7*, 6023–6032. [[CrossRef](#)]
117. Teresita, V.M.; Manikandan, A.; Josephine, B.A.; Sujatha, S.; Antony, S.A. Electromagnetic Properties and Humidity-Sensing Studies of Magnetically Recoverable LaMg<sub>x</sub>Fe<sub>1-x</sub>O<sub>3-δ</sub> Perovskites Nano-photocatalysts by Sol-Gel Route. *J. Supercond. Nov. Magn.* **2016**, *29*, 1691–1701. [[CrossRef](#)]
118. Duan, Z.; Xu, M.; Li, T.; Zhang, Y.; Zou, H. Super-fast response humidity sensor based on La<sub>0.7</sub>Sr<sub>0.3</sub>MnO<sub>3</sub> nanocrystals prepared by PVP-assisted sol-gel method. *Sens. Actuators B* **2018**, *258*, 527–534. [[CrossRef](#)]
119. El-Ads, E.H.; Galal, A.; Atta, N.F. The effect of A-site doping in a strontium palladium perovskite and its applications for non-enzymatic glucose sensing. *RSC Adv.* **2016**, *6*, 16183–16196. [[CrossRef](#)]
120. He, J.; Sunarso, J.; Miao, J.; Sun, H.; Dai, J.; Zhang, C.; Zhou, W.; Shao, Z. A highly sensitive perovskite oxide sensor for detection of p-phenylenediamine in hair dyes. *J. Hazard. Mater.* **2019**, *369*, 699–706. [[CrossRef](#)] [[PubMed](#)]
121. Atta, N.F.; Galal, A.; El-Ads, E.H. Effect of B-site doping on Sr<sub>2</sub>PdO<sub>3</sub> perovskite catalyst activity for non-enzymatic determination of glucose in biological fluids. *J. Electroanal. Chem.* **2019**, *852*, 113523. [[CrossRef](#)]
122. Rosa Silva, E.; Nicolini, J.V.; Yamauchi, L.; Machado, T.M.; Curi, M.; Furtado, J.G.; Secchi, A.R.; Ferraz, H.C. Carbon-based electrode loaded with Y-doped SrTiO<sub>3</sub> perovskite as support for enzyme immobilization in biosensors. *Ceram. Int.* **2020**, *46*, 3592–3599. [[CrossRef](#)]
123. Kayhomayun, Z.; Ghani, K.; Zargoosh, K. Surfactant-assisted synthesis of fluorescent SmCrO<sub>3</sub> nanopowder and its application for fast detection of nitroaromatic and nitramine explosives in solution. *Mater. Chem. Phys.* **2020**, *247*, 122899. [[CrossRef](#)]
124. Hernández-Rodríguez, M.A.; Lozano-Gorrín, A.D.; Martín, I.R.; Rodríguez-Mendoza, U.R.; Lavín, V. Comparison of the sensitivity as optical temperature sensor of nano-perovskite doped with Nd<sup>3+</sup> ions in the first and second biological windows. *Sens. Actuators B* **2018**, *255*, 970–976. [[CrossRef](#)]
125. Michel, C.R.; López-Alvarez, M.A.; Martínez-Preciado, A.H.; Oleinikov, V. Ultraviolet Detection and Photocatalytic Activity of Nanostructured LaCoO<sub>3</sub> Prepared by Solution-Polymerization. *ECS J. Solid State Sci. Technol.* **2019**, *8*, Q9–Q14. [[CrossRef](#)]
126. Liang, J.; Chen, D.; Yao, X.; Zhang, K.; Qu, F.; Qin, L.; Huang, Y.; Li, J. Recent Progress and Development in Inorganic Halide Perovskite Quantum Dots for Photoelectrochemical Applications. *Small* **2020**, *16*, 1903398. [[CrossRef](#)] [[PubMed](#)]
127. Zeng, Z.; Xu, Y.; Zhang, Z.; Gao, Z.; Luo, M.; Yin, Z.; Zhang, C.; Xu, J.; Huang, B.; Luo, F.; et al. Rare-earth-containing perovskite nanomaterials: Design, synthesis, properties and applications. *Chem. Soc. Rev.* **2020**, *49*, 1109–1143. [[CrossRef](#)] [[PubMed](#)]
128. Aamir, M.; Sher, M.; Malik, M.A.; Revaprasadu, N.; Akhtar, J. A facile approach for selective and sensitive detection of aqueous contamination in DMF by using perovskite material. *Mater. Lett.* **2016**, *183*, 135–138. [[CrossRef](#)]
129. Zhou, L.; Liao, J.-F.; Huang, Z.-G.; Wei, J.-H.; Wang, X.-D.; Li, W.-G.; Chen, H.-Y.; Kuang, D.-B.; Su, C.-Y. A Highly Red-Emissive Lead-Free Indium-Based Perovskite Single Crystal for Sensitive Water Detection. *Angew. Chem. Int. Ed.* **2019**, *58*, 5277–5281. [[CrossRef](#)]
130. Sheng, X.; Liu, Y.; Wang, Y.; Li, Y.; Wang, X.; Wang, X.; Dai, Z.; Bao, J.; Xu, X. Cesium Lead Halide Perovskite Quantum Dots as a Photoluminescence Probe for Metal Ions. *Adv. Mater.* **2017**, *29*, 1700150. [[CrossRef](#)]
131. Liu, Y.; Tang, X.; Zhu, T.; Deng, M.; Ikechukwu, I.P.; Huang, W.; Yin, G.; Bai, Y.; Qu, D.; Huang, X.; et al. All-inorganic CsPbBr<sub>3</sub> perovskite quantum dots as a photoluminescent probe for ultrasensitive Cu<sup>2+</sup> detection. *J. Mater. Chem. C* **2018**, *6*, 4793–4799. [[CrossRef](#)]

132. Ding, N.; Zhou, D.; Pan, G.; Xu, W.; Chen, X.; Li, D.; Zhang, X.; Zhu, J.; Ji, Y.; Song, H. Europium-Doped Lead-Free Cs<sub>3</sub>Bi<sub>2</sub>Br<sub>9</sub> Perovskite Quantum Dots and Ultrasensitive Cu<sup>2+</sup> Detection. *ACS Sustain. Chem. Eng.* **2019**, *7*, 8397–8404. [[CrossRef](#)]
133. Halali, V.V.; Shwetha Rani, R.; Geetha Balakrishna, R.; Budagumpi, S. Ultra-trace level chemosensing of uranyl ions; scuffle between electron and energy transfer from perovskite quantum dots to adsorbed uranyl ions. *Microchem. J.* **2020**, *156*, 104808. [[CrossRef](#)]
134. Weng, Z.; Qin, J.; Umar, A.A.; Wang, J.; Zhang, X.; Wang, H.; Cui, X.; Li, X.; Zheng, L.; Zhan, Y. Lead-Free Cs<sub>2</sub>BiAgBr<sub>6</sub> Double Perovskite-Based Humidity Sensor with Superfast Recovery Time. *Adv. Funct. Mater.* **2019**, *29*, 1902234. [[CrossRef](#)]
135. Chen, H.; Zhang, M.; Fu, X.; Fusco, Z.; Bo, R.; Xing, B.; Nguyen, H.T.; Barugkin, C.; Zheng, J.; Lau, C.F.J.; et al. Light-activated inorganic CsPbBr<sub>2</sub>I perovskite for room-temperature self-powered chemical sensing. *Phys. Chem. Chem. Phys.* **2019**, *21*, 24187–24193. [[CrossRef](#)] [[PubMed](#)]
136. Protesescu, L.; Yakunin, S.; Bodnarchuk, M.I.; Krieg, F.; Caputo, R.; Hendon, C.H.; Yang, R.X.; Walsh, A.; Kovalenko, M.V. Nanocrystals of Cesium Lead Halide Perovskites (CsPbX<sub>3</sub>, X = Cl, Br, and I): Novel Optoelectronic Materials Showing Bright Emission with Wide Color Gamut. *Nano Lett.* **2015**, *15*, 3692–3696. [[CrossRef](#)] [[PubMed](#)]
137. Chen, H.; Zhang, M.; Bo, R.; Barugkin, C.; Zheng, J.; Ma, Q.; Huang, S.; Ho-Baillie, A.W.Y.; Catchpole, K.R.; Tricoli, A. Superior Self-Powered Room-Temperature Chemical Sensing with Light-Activated Inorganic Halides Perovskites. *Small* **2018**, *14*, 1702571. [[CrossRef](#)]
138. Chen, X.; Hu, H.; Xia, Z.; Gao, W.; Gou, W.; Qu, Y.; Ma, Y. CsPbBr<sub>3</sub> perovskite nanocrystals as highly selective and sensitive spectrochemical probes for gaseous HCl detection. *J. Mater. Chem. C* **2017**, *5*, 309–313. [[CrossRef](#)]
139. Chen, C.; Cai, Q.; Luo, F.; Dong, N.; Guo, L.; Qiu, B.; Lin, Z. Sensitive Fluorescent Sensor for Hydrogen Sulfide in Rat Brain Microdialysis via CsPbBr<sub>3</sub> Quantum Dots. *Anal. Chem.* **2019**, *91*, 15915–15921. [[CrossRef](#)]
140. Huang, H.; Hao, M.; Song, Y.; Dang, S.; Liu, X.; Dong, Q. Dynamic Passivation in Perovskite Quantum Dots for Specific Ammonia Detection at Room Temperature. *Small* **2020**, *16*, 1904462. [[CrossRef](#)]
141. Brintakis, K.; Gagaoudakis, E.; Kostopoulou, A.; Faka, V.; Argyrou, A.; Binas, V.; Kiriakidis, G.; Stratakis, E. Ligand-free all-inorganic metal halide nanocrystals for fast, ultra-sensitive and self-powered ozone sensors. *Nanoscale Adv.* **2019**, *1*, 2699–2706. [[CrossRef](#)]
142. Chen, X.; Sun, C.; Liu, Y.; Yu, L.; Zhang, K.; Asiri, A.M.; Marwani, H.M.; Tan, H.; Ai, Y.; Wang, X.; et al. All-inorganic perovskite quantum dots CsPbX<sub>3</sub> (Br/I) for highly sensitive and selective detection of explosive picric acid. *Chem. Eng. J.* **2020**, *379*, 122360. [[CrossRef](#)]
143. Niu, Y.; Zhang, F.; Bai, Z.; Dong, Y.; Yang, J.; Liu, R.; Zou, B.; Li, J.; Zhong, H. Aggregation-Induced Emission Features of Organometal Halide Perovskites and Their Fluorescence Probe Applications. *Adv. Opt. Mater.* **2015**, *3*, 112–119. [[CrossRef](#)]
144. Muthu, C.; Nagamma, S.R.; Nair, V.C. Luminescent hybrid perovskite nanoparticles as a new platform for selective detection of 2,4,6-trinitrophenol. *RSC Adv.* **2014**, *4*, 55908–55911. [[CrossRef](#)]
145. Xu, W.; Li, F.; Cai, Z.; Wang, Y.; Luo, F.; Chen, X. An ultrasensitive and reversible fluorescence sensor of humidity using perovskite CH<sub>3</sub>NH<sub>3</sub>PbBr<sub>3</sub>. *J. Mater. Chem. C* **2016**, *4*, 9651–9655. [[CrossRef](#)]
146. Ren, K.; Huang, L.; Yue, S.; Lu, S.; Liu, K.; Azam, M.; Wang, Z.; Wei, Z.; Qu, S.; Wang, Z. Turning a disadvantage into an advantage: Synthesizing high-quality organometallic halide perovskite nanosheet arrays for humidity sensors. *J. Mater. Chem. C* **2017**, *5*, 2504–2508. [[CrossRef](#)]
147. Gao, W.; Leng, M.; Hu, Z.; Li, J.; Li, D.; Liu, H.; Gao, L.; Niu, G.; Tang, J. Reversible luminescent humidity chromism of organic–inorganic hybrid PEA<sub>2</sub>MnBr<sub>4</sub> single crystals. *Dalton Trans.* **2020**, *49*, 5662–5668. [[CrossRef](#)]
148. Lu, L.-Q.; Tan, T.; Tian, X.-K.; Li, Y.; Deng, P. Visual and sensitive fluorescent sensing for ultratrace mercury ions by perovskite quantum dots. *Anal. Chim. Acta* **2017**, *986*, 109–114. [[CrossRef](#)]
149. Ma, C.; Lo, M.-F.; Lee, C.-S. Stabilization of organometallic halide perovskite nanocrystals in aqueous solutions and their applications in copper ion detection. *Chem. Commun.* **2018**, *54*, 5784–5787. [[CrossRef](#)]
150. Li, C.-H.; Liao, M.-Y.; Chen, C.-H.; Chueh, C.-C. Recent progress of anion-based 2D perovskites with different halide substitutions. *J. Mater. Chem. C* **2020**, *8*, 4294–4302. [[CrossRef](#)]
151. Lu, L.-Q.; Ma, M.-Y.; Tan, T.; Tian, X.-K.; Zhou, Z.-X.; Yang, C.; Li, Y. Novel dual ligands capped perovskite quantum dots for fluoride detection. *Sens. Actuators B* **2018**, *270*, 291–297. [[CrossRef](#)]

152. Kim, S.-H.; Kirakosyan, A.; Choi, J.; Kim, J.H. Detection of volatile organic compounds (VOCs), aliphatic amines, using highly fluorescent organic-inorganic hybrid perovskite nanoparticles. *Dyes Pigments* **2017**, *147*, 1–5. [[CrossRef](#)]
153. Li, M.; Zhou, J.; Molokeev, M.S.; Jiang, X.; Lin, Z.; Zhao, J.; Xia, Z. Lead-Free Hybrid Metal Halides with a Green-Emissive [MnBr<sub>4</sub>] Unit as a Selective Turn-On Fluorescent Sensor for Acetone. *Inorg. Chem.* **2019**, *58*, 13464–13470. [[CrossRef](#)]
154. Zhu, M.-Y.; Zhang, L.-X.; Yin, J.; Chen, J.-J.; Bie, L.-J. Ppt-level benzene detection and gas sensing mechanism using (C<sub>4</sub>H<sub>9</sub>NH<sub>3</sub>)<sub>2</sub>PbI<sub>2</sub>Br<sub>2</sub> organic–inorganic layered perovskite. *Inorg. Chem. Front.* **2018**, *5*, 3046–3052. [[CrossRef](#)]
155. Nur'aini, A.; Oh, I. Volatile organic compound gas sensors based on methylammonium lead iodide perovskite operating at room temperature. *RSC Adv.* **2020**, *10*, 12982–12987. [[CrossRef](#)]
156. Bao, C.; Yang, J.; Zhu, W.; Zhou, X.; Gao, H.; Li, F.; Fu, G.; Yu, T.; Zou, Z. A resistance change effect in perovskite CH<sub>3</sub>NH<sub>3</sub>PbI<sub>3</sub> films induced by ammonia. *Chem. Commun.* **2015**, *51*, 15426–15429. [[CrossRef](#)] [[PubMed](#)]
157. Maity, A.; Raychaudhuri, A.K.; Ghosh, B. High sensitivity NH<sub>3</sub> gas sensor with electrical readout made on paper with perovskite halide as sensor material. *Sci. Rep.* **2019**, *9*, 7777. [[CrossRef](#)] [[PubMed](#)]
158. Sheikh, A.D.; Vhanalakar, V.; Katware, A.; Pawar, K.; Patil, P.S. Two-Step Antisolvent Precipitated MAPbI<sub>3</sub>-Pellet-Based Robust Room-Temperature Ammonia Sensor. *Adv. Mater. Technol.* **2019**, *4*, 1900251. [[CrossRef](#)]
159. Jiao, W.; He, J.; Zhang, L. Synthesis and high ammonia gas sensitivity of (CH<sub>3</sub>NH<sub>3</sub>)PbBr<sub>3-x</sub>I<sub>x</sub> perovskite thin film at room temperature. *Sens. Actuators B* **2020**, *309*, 127786. [[CrossRef](#)]
160. Li, G.; Zhang, W.; She, C.; Jia, S.; Liu, S.; Yue, F.; Jing, C.; Cheng, Y.; Chu, J. Stable fluorescent NH<sub>3</sub> sensor based on MAPbBr<sub>3</sub> encapsulated by tetrabutylammonium cations. *J. Alloys Compd.* **2020**, *835*, 155386. [[CrossRef](#)]
161. Zhang, B.; Zhou, S.; Tong, L.; Liao, Y.; Yi, J.; Qi, Y.; Yao, J. Large scale quantum dynamics investigations on the sensing mechanism of H<sub>2</sub>O, acetone, NO<sub>2</sub> and O<sub>3</sub> adsorption on the (MA)<sub>2</sub>Pb(SCN)<sub>2</sub>I<sub>2</sub> surface. *Phys. Chem. Chem. Phys.* **2019**, *21*, 21223–21235. [[CrossRef](#)]
162. Zhuang, Y.; Yuan, W.; Qian, L.; Chen, S.; Shi, G. High-performance gas sensors based on a thiocyanate ion-doped organometal halide perovskite. *Phys. Chem. Chem. Phys.* **2017**, *19*, 12876–12881. [[CrossRef](#)]
163. Fu, X.; Jiao, S.; Dong, N.; Lian, G.; Zhao, T.; Lv, S.; Wang, Q.; Cui, D. A CH<sub>3</sub>NH<sub>3</sub>PbI<sub>3</sub> film for a room-temperature NO<sub>2</sub> gas sensor with quick response and high selectivity. *RSC Adv.* **2018**, *8*, 390–395. [[CrossRef](#)]
164. Zhu, R.; Zhang, Y.; Zhong, H.; Wang, X.; Xiao, H.; Chen, Y.; Li, X. High-performance room-temperature NO<sub>2</sub> sensors based on CH<sub>3</sub>NH<sub>3</sub>PbBr<sub>3</sub> semiconducting films: Effect of surface capping by alkyl chain on sensor performance. *J. Phys. Chem. Solids* **2019**, *129*, 270–276. [[CrossRef](#)]
165. Hien, V.X.; Hung, P.T.; Han, J.; Lee, S.; Lee, J.-H.; Heo, Y.-W. Growth and gas sensing properties of methylammonium tin iodide thin film. *Scr. Mater.* **2020**, *178*, 108–113. [[CrossRef](#)]
166. Chen, H.; Zhang, M.; Xing, B.; Fu, X.; Bo, R.; Mulmudi, H.K.; Huang, S.; Ho-Baillie, A.W.Y.; Catchpole, K.R.; Tricoli, A. Superior Self-Charged and -Powered Chemical Sensing with High Performance for NO<sub>2</sub> Detection at Room Temperature. *Adv. Opt. Mater.* **2020**, *8*, 1901863. [[CrossRef](#)]
167. Stoeckel, M.-A.; Gobbi, M.; Bonacchi, S.; Liscio, F.; Ferlauto, L.; Orgiu, E.; Samorì, P. Reversible, Fast, and Wide-Range Oxygen Sensor Based on Nanostructured Organometal Halide Perovskite. *Adv. Mater.* **2017**, *29*, 1702469. [[CrossRef](#)]
168. Kakavelakis, G.; Gagaoudakis, E.; Petridis, K.; Petromichelaki, V.; Binas, V.; Kiriakidis, G.; Kymakis, E. Solution Processed CH<sub>3</sub>NH<sub>3</sub>PbI<sub>3-x</sub>Cl<sub>x</sub> Perovskite Based Self-Powered Ozone Sensing Element Operated at Room Temperature. *ACS Sens.* **2018**, *3*, 135–142. [[CrossRef](#)] [[PubMed](#)]
169. Gagaoudakis, E.; Panagiotopoulos, A.; Maksudov, T.; Moschogiannaki, M.; Katerinopoulou, D.; Kakavelakis, G.; Kiriakidis, G.; Binas, V.; Kymakis, E.; Petridis, K. Self-powered, flexible and room temperature operated solution processed hybrid metal halide p-type sensing element for efficient hydrogen detection. *J. Phys. Mater.* **2020**, *3*, 014010. [[CrossRef](#)]
170. Bansode, U.; Ogale, S. On-axis pulsed laser deposition of hybrid perovskite films for solar cell and broadband photo-sensor applications. *J. Appl. Phys.* **2017**, *121*, 133107. [[CrossRef](#)]

171. Xia, M.; Yuan, J.-H.; Luo, J.; Pan, W.; Wu, H.; Chen, Q.; Xue, K.-H.; Miao, X.; Niu, G.; Tang, J. Two-dimensional perovskites as sensitive strain sensors. *J. Mater. Chem. C* **2020**, *8*, 3814–3820. [[CrossRef](#)]
172. Saraf, R.; Pu, L.; Maheshwari, V. A Light Harvesting, Self-Powered Monolith Tactile Sensor Based on Electric Field Induced Effects in MAPbI<sub>3</sub> Perovskite. *Adv. Mater.* **2018**, *30*, 1705778. [[CrossRef](#)]
173. Saraf, R.; Tsui, T.; Maheshwari, V. Modulation of mechanical properties and stable light energy harvesting by poling in polymer integrated perovskite films: A wide range, linear and highly sensitive tactile sensor. *J. Mater. Chem. A* **2019**, *7*, 14192–14198. [[CrossRef](#)]
174. Chen, D.; Yi, J. One-pot electrospinning and gas-sensing properties of LaMnO<sub>3</sub> perovskite/SnO<sub>2</sub> heterojunction nanofibers. *J. Nanopart. Res.* **2018**, *20*, 65. [[CrossRef](#)]
175. Zhou, T.; Zhang, T.; Zhang, R.; Lou, Z.; Deng, J.; Lu, G.; Wang, L. Constructing p–n heterostructures for efficient structure-driven ethanol sensing performance. *Sens. Actuators B* **2018**, *255*, 745–753. [[CrossRef](#)]
176. Chen, M.; Wang, H.; Hu, J.; Zhang, Y.; Li, K.; Zhang, D.; Zhou, S.; Zhang, J.; Zhu, Z.; Liu, Q. Near-Room-Temperature Ethanol Gas Sensor Based on Mesoporous Ag/Zn–LaFeO<sub>3</sub> Nanocomposite. *Adv. Mater. Interfaces* **2019**, *6*, 1801453. [[CrossRef](#)]
177. Zhang, N.; Ruan, S.; Yin, Y.; Li, F.; Wen, S.; Chen, Y. Self-Sacrificial Template-Driven LaFeO<sub>3</sub>/α-Fe<sub>2</sub>O<sub>3</sub> Porous Nano-Octahedrons for Acetone Sensing. *ACS Appl. Nano Mater.* **2018**, *1*, 4671–4681. [[CrossRef](#)]
178. Kang, J.-Y.; Jang, J.-S.; Koo, W.-T.; Seo, J.; Choi, Y.; Kim, M.-H.; Kim, D.-H.; Cho, H.-J.; Jung, W.; Kim, I.-D. Perovskite La<sub>0.75</sub>Sr<sub>0.25</sub>Cr<sub>0.5</sub>Mn<sub>0.5</sub>O<sub>3–δ</sub> sensitized SnO<sub>2</sub> fiber-in-tube scaffold: Highly selective and sensitive formaldehyde sensing. *J. Mater. Chem. A* **2018**, *6*, 10543–10551. [[CrossRef](#)]
179. Du, L.; Zhang, H.; Zhu, M.; Zhang, M. Construction of flower-like ZnSnO<sub>3</sub>/Zn<sub>2</sub>SnO<sub>4</sub> hybrids for enhanced phenylamine sensing performance. *Inorg. Chem. Front.* **2019**, *6*, 2311–2317. [[CrossRef](#)]
180. Zhang, Y.; Zou, H.; Peng, J.; Duan, Z.; Ma, M.; Xin, X.; Li, W.; Zheng, X. Enhanced humidity sensing properties of SmFeO<sub>3</sub>-modified MoS<sub>2</sub> nanocomposites based on the synergistic effect. *Sens. Actuators B* **2018**, *272*, 459–467. [[CrossRef](#)]
181. Lin, H.-J.; Baltrus, J.P.; Gao, H.; Ding, Y.; Nam, C.-Y.; Ohodnicki, P.; Gao, P.-X. Perovskite Nanoparticle-Sensitized Ga<sub>2</sub>O<sub>3</sub> Nanorod Arrays for CO Detection at High Temperature. *ACS Appl. Mater. Interfaces* **2016**, *8*, 8880–8887. [[CrossRef](#)]
182. Joshi, S.; Ippolito, S.J.; Periasamy, S.; Sabri, Y.M.; Sunkara, M.V. Efficient Heterostructures of Ag@CuO/BaTiO<sub>3</sub> for Low-Temperature CO<sub>2</sub> Gas Detection: Assessing the Role of Nanointerfaces during Sensing by Operando DRIFTS Technique. *ACS Appl. Mater. Interfaces* **2017**, *9*, 27014–27026. [[CrossRef](#)]
183. Joshi, S.; Antolasic, F.; Sunkara, M.V.; Bhargava, S.K.; Ippolito, S.J. Highly Selective CO<sub>2</sub> Gas Sensing Properties of CaO–BaTiO<sub>3</sub> Heterostructures Effectuated through Discretely Created n–n Nanointerfaces. *ACS Sustain. Chem. Eng.* **2018**, *6*, 4086–4097. [[CrossRef](#)]
184. Joshi, S.; Canjeevaram Balasubramanyam, R.K.; Ippolito, S.J.; Sabri, Y.M.; Kandjani, A.E.; Bhargava, S.K.; Sunkara, M.V. Straddled Band Aligned CuO/BaTiO<sub>3</sub> Heterostructures: Role of Energetics at Nanointerface in Improving Photocatalytic and CO<sub>2</sub> Sensing Performance. *ACS Appl. Nano Mater.* **2018**, *1*, 3375–3388. [[CrossRef](#)]
185. Yin, X.-T.; Dastan, D.; Wu, F.-Y.; Li, J. Facile Synthesis of SnO<sub>2</sub>/LaFeO<sub>3–x</sub>N<sub>x</sub> Composite: Photocatalytic Activity and Gas Sensing Performance. *Nanomaterials* **2019**, *9*, 1163. [[CrossRef](#)] [[PubMed](#)]
186. Zhang, B.; Lin, H.-J.; Gao, H.; Lu, X.; Nam, C.-Y.; Gao, P.-X. Perovskite-sensitized β-Ga<sub>2</sub>O<sub>3</sub> nanorod arrays for highly selective and sensitive NO<sub>2</sub> detection at high temperature. *J. Mater. Chem. A* **2020**, *8*, 10845–10854. [[CrossRef](#)]
187. El-Ads, E.H.; Atta, N.F.; Galal, A.; El-Gohary, A.R.M. Nano-perovskite decorated carbon nanotubes composite for ultrasensitive determination of a cardio-stimulator drug. *J. Electroanal. Chem.* **2018**, *816*, 149–159. [[CrossRef](#)]
188. Alluri, N.R.; Purusothaman, Y.; Chandrasekhar, A.; Kim, S.-J. Self-powered wire type UV sensor using in-situ radial growth of BaTiO<sub>3</sub> and TiO<sub>2</sub> nanostructures on human hair sized single Ti-wire. *Chem. Eng. J.* **2018**, *334*, 1729–1739. [[CrossRef](#)]
189. Wang, Y.; Ding, G.; Mao, J.-Y.; Zhou, Y.; Han, S.-T. Recent advances in synthesis and application of perovskite quantum dot based composites for photonics, electronics and sensors. *Sci. Technol. Adv. Mater.* **2020**, *21*, 278–302. [[CrossRef](#)]

190. Wang, Y.; Zhu, Y.; Huang, J.; Cai, J.; Zhu, J.; Yang, X.; Shen, J.; Li, C. Perovskite quantum dots encapsulated in electrospun fiber membranes as multifunctional supersensitive sensors for biomolecules, metal ions and pH. *Nanoscale Horiz.* **2017**, *2*, 225–232. [[CrossRef](#)]
191. Zhang, D.; Xu, Y.; Liu, Q.; Xia, Z. Encapsulation of  $\text{CH}_3\text{NH}_3\text{PbBr}_3$  Perovskite Quantum Dots in MOF-5 Microcrystals as a Stable Platform for Temperature and Aqueous Heavy Metal Ion Detection. *Inorg. Chem.* **2018**, *57*, 4613–4619. [[CrossRef](#)]
192. Shan, X.; Zhang, S.; Zhou, M.; Geske, T.; Davis, M.; Hao, A.; Wang, H.; Yu, Z. Porous Halide Perovskite–Polymer Nanocomposites for Explosive Detection with a High Sensitivity. *Adv. Mater. Interfaces* **2019**, *6*, 1801686. [[CrossRef](#)]
193. Casanova-Cháfer, J.; García-Aboal, R.; Atienzar, P.; Llobet, E. Gas Sensing Properties of Perovskite Decorated Graphene at Room Temperature. *Sensors* **2019**, *19*, 4563. [[CrossRef](#)]
194. Zhang, X.; Sun, Y.; Fan, Y.; Liu, Z.; Zeng, Z.; Zhao, H.; Wang, X.; Xu, J. Effects of organotin halide perovskite and Pt nanoparticles in  $\text{SnO}_2$ -based sensing materials on the detection of formaldehyde. *J. Mater. Sci. Mater. Electron.* **2019**, *30*, 20624–20637. [[CrossRef](#)]
195. Huang, S.; Guo, M.; Tan, J.; Geng, Y.; Wu, J.; Tang, Y.; Su, C.; Lin, C.C.; Liang, Y. Novel Fluorescence Sensor Based on All-Inorganic Perovskite Quantum Dots Coated with Molecularly Imprinted Polymers for Highly Selective and Sensitive Detection of Omethoate. *ACS Appl. Mater. Interfaces* **2018**, *10*, 39056–39063. [[CrossRef](#)]
196. Tan, L.; Guo, M.; Tan, J.; Geng, Y.; Huang, S.; Tang, Y.; Su, C.; Lin, C.; Liang, Y. Development of high-luminescence perovskite quantum dots coated with molecularly imprinted polymers for pesticide detection by slowly hydrolysing the organosilicon monomers in situ. *Sens. Actuators B* **2019**, *291*, 226–234. [[CrossRef](#)]
197. Chen, X.; Li, D.; Pan, G.; Zhou, D.; Xu, W.; Zhu, J.; Wang, H.; Chen, C.; Song, H. All-inorganic perovskite quantum dot/ $\text{TiO}_2$  inverse opal electrode platform: Stable and efficient photoelectrochemical sensing of dopamine under visible irradiation. *Nanoscale* **2018**, *10*, 10505–10513. [[CrossRef](#)] [[PubMed](#)]
198. Nikolaou, P.; Vassilakopoulou, A.; Papadatos, D.; Topoglidis, E.; Koutselas, I. A chemical sensor for  $\text{CBr}_4$  based on quasi-2D and 3D hybrid organic–inorganic perovskites immobilized on  $\text{TiO}_2$  films. *Mater. Chem. Front.* **2018**, *2*, 730–740. [[CrossRef](#)]
199. Yang, X.; Chen, L.; Xiong, X.; Shu, Y.; Jin, D.; Zang, Y.; Wang, W.; Xu, Q.; Hu, X.-Y. Molecularly imprinted polymers and PEG double engineered perovskite: An efficient platform for constructing aqueous solution feasible photoelectrochemical sensor. *Sens. Actuators B* **2020**, *304*, 127321. [[CrossRef](#)]
200. Li, Q.; Wang, H.; Yue, X.; Du, J. Perovskite nanocrystals fluorescence nanosensor for ultrasensitive detection of trace melamine in dairy products by the manipulation of inner filter effect of gold nanoparticles. *Talanta* **2020**, *211*, 120705. [[CrossRef](#)]
201. Tang, X.; Zu, Z.; Zang, Z.; Hu, Z.; Hu, W.; Yao, Z.; Chen, W.; Li, S.; Han, S.; Zhou, M.  $\text{CsPbBr}_3$ /Reduced Graphene Oxide nanocomposites and their enhanced photoelectric detection application. *Sens. Actuators B* **2017**, *245*, 435–440. [[CrossRef](#)]
202. Lou, S.; Zhou, Z.; Xuan, T.; Li, H.; Jiao, J.; Zhang, H.; Gautier, R.; Wang, J. Chemical Transformation of Lead Halide Perovskite into Insoluble, Less Cytotoxic, and Brightly Luminescent  $\text{CsPbBr}_3/\text{CsPb}_2\text{Br}_5$  Composite Nanocrystals for Cell Imaging. *ACS Appl. Mater. Interfaces* **2019**, *11*, 24241–24246. [[CrossRef](#)]
203. Wang, Y.; Yu, D.; Wang, Z.; Li, X.; Chen, X.; Nalla, V.; Zeng, H.; Sun, H. Solution-Grown  $\text{CsPbBr}_3/\text{Cs}_4\text{PbBr}_6$  Perovskite Nanocomposites: Toward Temperature-Insensitive Optical Gain. *Small* **2017**, *13*, 1701587. [[CrossRef](#)]
204. Huang, Y.; Wang, S.; Zhu, Y.; Li, F.; Jin, J.; Dong, J.; Lin, F.; Wang, Y.; Chen, X. Dual-Mode of Fluorescence Turn-On and Wavelength-Shift for Methylamine Gas Sensing Based on Space-Confined Growth of Methylammonium Lead Tribromide Perovskite Nanocrystals. *Anal. Chem.* **2020**, *92*, 5661–5665. [[CrossRef](#)]
205. Jacky, E.; Soline, B.-R.; Marcelo, C.; Laurent, P.; Jean-Marc, J.; Claudine, K. Theoretical insights into hybrid perovskites for photovoltaic applications. *Proc. SPIE* **2016**, *9742*, 97421A.
206. Brakkee, R.; Williams, R.M. Minimizing Defect States in Lead Halide Perovskite Solar Cell Materials. *Appl. Sci.* **2020**, *10*, 3061. [[CrossRef](#)]
207. Li, X.; Dan, Y.; Dong, R.; Cao, Z.; Niu, C.; Song, Y.; Li, S.; Hu, J. Computational Screening of New Perovskite Materials Using Transfer Learning and Deep Learning. *Appl. Sci.* **2019**, *9*, 5510. [[CrossRef](#)]

208. Tripathi, K.M.; Kim, T.; Losic, D.; Tung, T.T. Recent advances in engineered graphene and composites for detection of volatile organic compounds (VOCs) and non-invasive diseases diagnosis. *Carbon* **2016**, *110*, 97–129. [[CrossRef](#)]
209. Tripathi, K.M.; Sachan, A.; Castro, M.; Choudhary, V.; Sonkar, S.K.; Feller, J.F. Green carbon nanostructured quantum resistive sensors to detect volatile biomarkers. *Sustain. Mater. Technol.* **2018**, *16*, 1–11. [[CrossRef](#)]
210. Das, G.S.; Shim, J.P.; Bhatnagar, A.; Tripathi, K.M.; Kim, T. Biomass-derived Carbon Quantum Dots for Visible-Light-Induced Photocatalysis and Label-Free Detection of Fe(III) and Ascorbic acid. *Sci. Rep.* **2019**, *9*, 15084. [[CrossRef](#)] [[PubMed](#)]
211. Sharma, A.; Sharma, N.; Kumari, A.; Lee, H.-J.; Kim, T.; Tripathi, K.M. Nano-carbon based sensors for bacterial detection and discrimination in clinical diagnosis: A junction between material science and biology. *Appl. Mater. Today* **2020**, *18*, 100467. [[CrossRef](#)]



© 2020 by the authors. Licensee MDPI, Basel, Switzerland. This article is an open access article distributed under the terms and conditions of the Creative Commons Attribution (CC BY) license (<http://creativecommons.org/licenses/by/4.0/>).